VIETNAM NATIONAL UNIVERSITY, HANOI
UNIVERSITY OF SCIENCE
FACULTY OF PHYSICS
****

PHAM THI TUYET NHUNG

PERFORMANCE STUDIES OF
WATER CHERENKOV COUNTERS

MASTER THESIS

Hanoi - 2006

VIETNAM NATIONAL UNIVERSITY, HANOI
UNIVERSITY OF SCIENCE
FACULTY OF PHYSICS
****

PHAM THI TUYET NHUNG

PERFORMANCE STUDIES OF WATER CHERENKOV COUNTERS

(NGHIÊN CỨU CHẤT LƯỢNG HỆ ĐẾM TRERENKOV NƯỚC)

MASTER THESIS
NUCLEAR PHYSICS
CODE: 1.02.03

SUPERVISOR: Prof. PIERRE DARRIULAT

Hanoi - 2006

Abstract

Studies of the operation and performance of the water Cherenkov counters used in the Pierre Auger Observatory are presented. They include in particular a study of the response of such a counter to atmospheric muons using a replica of the Auger counters constructed for this purpose at VATLY (Hanoi). They also present an analysis of signals recorded at the Pierre Auger Observatory with the aim of separating their muon and electron-photon components, an important tool in the identification of the primary cosmic rays.

PREAMBLE

Contents

Chapter 1 - OVERVIEW OF THE PIERRE AUGER OBSERVATORY AND ITS SURFACE DETECTOR

1.1 Introduction

Although the existence of cosmic rays has been known for nearly one century, they are still of astrophysical interest [1,2]. Cosmic rays are mostly charged particles that travel in space up to extremely high energies ~10^{20} eV. Their flux has a power law energy spectrum (Fig. 1.1) that covers over 32 decades (12 decades in energy), and is approximately proportional to $E^{-2.7}$. Today, no theory is able to reproduce accurately this distribution, a fortiori to account for details such as the two breaks observed around 10^{15} eV and 10^{19} eV respectively, referred to as the "knee" and the "ankle". In the knee region, extragalactic cosmic rays start having enough energy to overcome the barrier resulting from the presence of magnetic field in the galaxy, approximately at the microgauss level. There, the cosmic ray flux is very low, 1 particle/km²/sr/year and above 10^{20} eV it is only 1particle/km²/sr/century. Such low rates have made it difficult to accumulate adequate statistics in the energy range of these ultra high energy cosmic rays (UHECR).
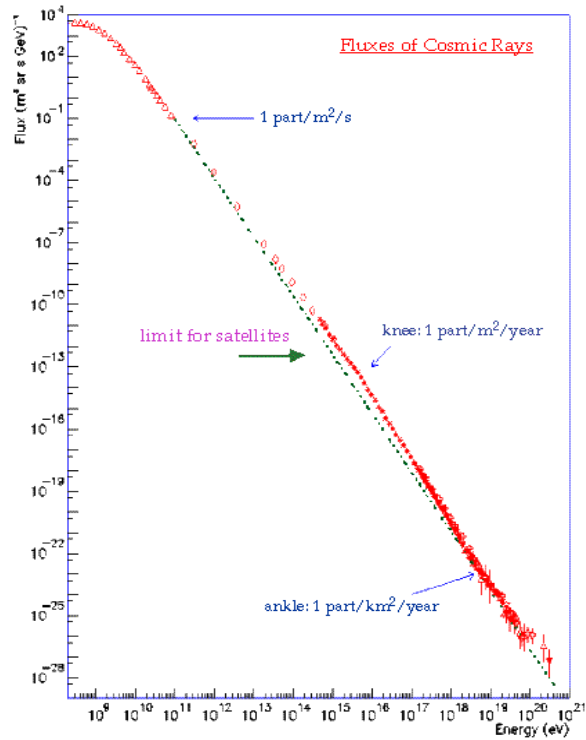
Figure 1.1 Cosmic ray energy spectrum.

Thanks to recent results of X-ray and gamma-ray astronomy, one believes that galactic supernova remnants are important sources of high energy cosmic rays up to 10^{14}eV and that acceleration takes place on the shock front [3]. In the region above the "knee", because of the extremely high energies, a similar acceleration mechanism would require sources being the site of very violent events, such as Active Galactic Nuclei or Gamma Ray Bursts. Unfortunately, pointing back to the

sources of charged cosmic rays is made difficult by the presence of magnetic fields along their path. Only in the UHECR range may one hope that the induced smearing will not exceed a few degrees.

UHECRs are observed from the extensive air showers that they produce when entering the Earth atmosphere. There exist two main methods of detection, one consists in sampling the particle density on ground and the other in detecting the fluorescence light produced on nitrogen molecules along the shower [1,2]. These methods have been used, or are being used, by several experiments such as Volcano Ranch, Haverah Park and AGASA for the surface detector arrays, and Fly's Eye and HiRes for fluorescence detectors. However the two largest experiments, AGASA [4] and HiRes [5], did not give a consistent picture of the energy spectrum at the highest energies (Fig. 1.2). This discrepancy may be due to systematic differences in reconstructing the energy from the measurements using ground arrays and fluorescence detectors.
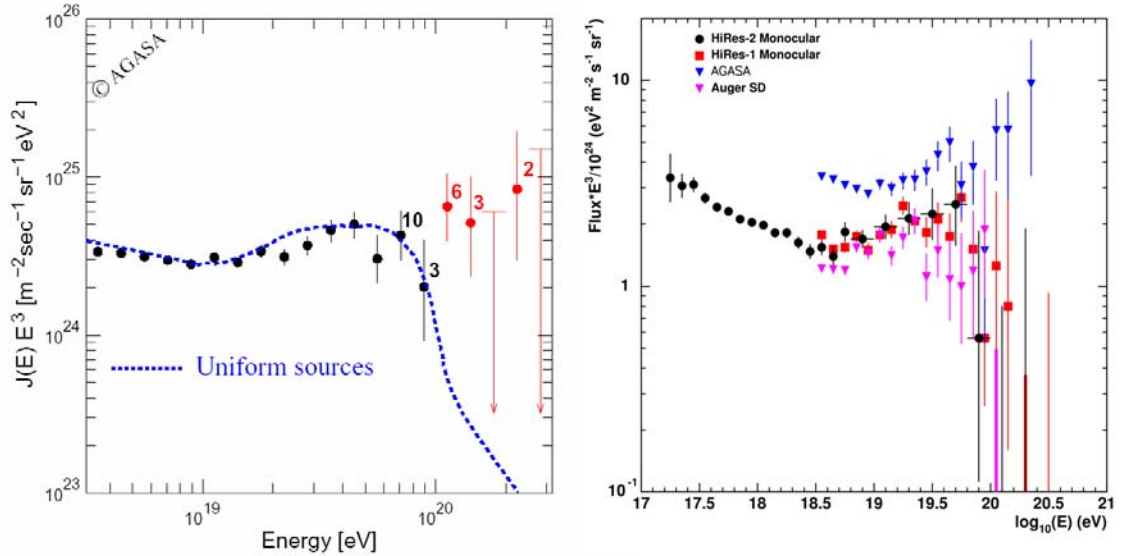
Figure 1.2 Left: Differential energy spectrum ($\times E^3$) from the AGASA experiment. The dotted line is the result of a simulation in the region of the GZK cut-off.
Right: Combined differential energy spectra ($\times E^3/10^{24}$) from the HiRes (1 and 2 monocular), AGASA and Auger (SD) experiments.

The Pierre Auger Observatory (PAO) is a giant hybrid detector [6] combining the strengths of both surface detector arrays and fluorescence detectors [7] with the aim to study the high end of the cosmic ray energy spectrum with

improved statistics and reliability. It is currently under construction in the Argentina pampas [8]. Preliminary results [9] are shown on Figure 1.2.

1.2 The main physics of the Pierre Auger Observatory

The main physics goal of the PAO is a study the high end of the energy spectrum. This will provide an accurate measurement of the flux that will settle the GZK controversy (see below), will hopefully identify the brightest sources and clarify the nature – protons, nuclei, or else – of the UHECRs.

Above 10^{20}eV or so one expects the spectrum to be cut off (this is known as the Greisen-Zatsepin-Kuzmin or GZK cutoff) because of the interactions between the cosmic ray particles with the 2.7K Cosmic Microwave Background (CMB) photons [10,11]. In the case of incident nuclei, the resulting distortion of the primary spectrum depends on several parameters: the reactions considered and their cross-sections, essentially $p\gamma \rightarrow \pi^{0(+)}p(n)$ or $n\gamma \rightarrow \pi^{-(0)}p(n)$ either directly or via $\Delta^+(\Delta^0)$ production[1]; the distribution of the CMB photons in energy ε (Planck spectrum) and momentum (isotropic); the incident energy distribution of the primary nucleus. For a given initial state, defined by the energy E of the primary nucleon and the angle θ between its momentum and that of the CMB photon, the kinematics of the reaction gives $M_N \Delta m \cong E\varepsilon (1 - cos\theta)$ where Δm is the difference between the mass of the final state and the nucleon mass, namely either the pion mass (140 MeV) or the difference (290 MeV) between the delta mass and the nucleon mass M_N. For a given Δm, the energy distribution of the final state proton is obtained by integration over incident energy and over ε and θ with weights accounting for the CMB energy distribution and for the ε and θ dependences of the cross-section. To get a crude order of magnitude estimate of the effect, we may replace the Planck spectrum by a δ-function at 2.7K ~ 2.3×10^{-3}eV, consider only head-on collisions, $cos\theta = -1$, and assume that any interacting nucleon is essentially lost (namely that its energy is shifted to a much lower range where its contribution to the spectrum is negligible). This results in an abrupt threshold at $M_N\Delta m/2\varepsilon = 5.8×10^{20}$ eV and 2.9×10^{20} eV for Δ and π production respectively above which all nucleons that have interacted are suppressed. The fraction of surviving

---

[1] The neutron lifetime, for a γ of 10^{11}, is 10^{14}s, namely 2% of 50 Mpc. But once it has decayed, the neutron becomes a proton with very similar energy.

protons depends upon the reaction cross-section and the distance of the source (to which the target thickness, and therefore the interaction rate, is directly proportional). The exact calculation, taking all the above factors into account, gives instead [1] distortions illustrated in Figure 1.3. An essential result is that for source distances in excess of 50 Mpc the spectrum is effectively cut-off.
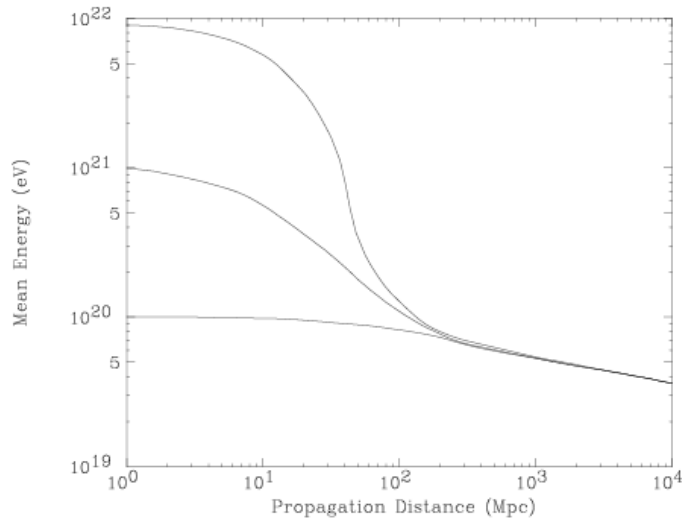
Figure 1.3 Mean energy of protons as a function of propagation distance through the CMB. Curves [1] are for energy at the source of 10^{22} eV, 10^{21} eV, and 10^{20} eV.

It is only for sources distant by less than 30 Mpc or so, that the effect of the cut-off is small. The observation of UHE protons above 10^{20}eV or so would therefore imply that they originate from sources located in the Milky Way or other nearby galaxies in the local cluster, restricting severely the possible acceleration mechanisms.

The angular resolution achieved in the PAO is ±0.6° for hybrid events. The deterioration due to the presence of magnetic field along the cosmic ray path is difficult to evaluate because little is known of the intergalactic fields, but reasonable estimates give some 10° in the 10^{19}eV region, which would be sufficient to identify the brightest sources [6].

Primaries are generally believed to be nuclei in the UHECR region as they are known to be at lower energies. However there exist speculations that explore the possibility that more exotic particles, such as very high mass relics of the GUT era, might be their source. Staying within the more conventional picture, it is important

to evaluate their elemental composition, namely to evaluate the relative abundance of protons and iron or other nuclei in their composition. This is a difficult task which relies on the fact that showers induced by heavier nuclei start to develop earlier than proton initiated showers. This cannot be observed on an event by event basis, but only statistically from the direct measurement of the longitudinal shower profile or from the muon to electron ratio on ground.

1.3 The Pierre Auger Observatory: its surface and fluorescence detectors

The PAO is designed to enable detailed studies of cosmic rays with energy above 10^{18} eV with high statistical significance. The observatory under current construction is located in the Argentina pampas and can explore the whole austral sky, including the center of the Milky Way. It is planned to build a second observatory in the northern hemisphere at a later stage.
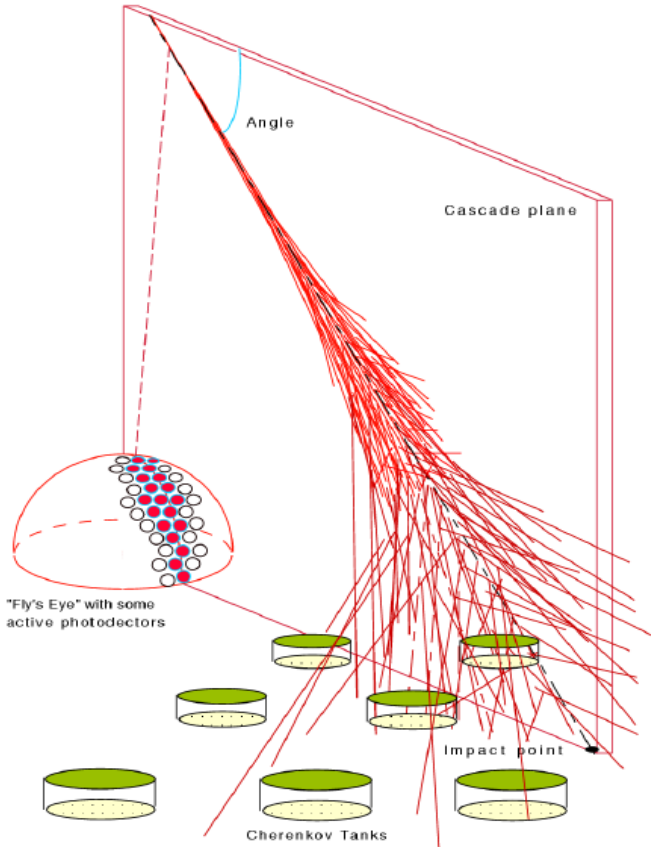

Figure 1.4 Schematic illustration of the hybrid concept of the Auger Observatory.

The PAO consists of a "hybrid" detector using both of the main detection techniques: a surface detector (SD) array to measure the lateral distribution and arrival time of the shower on ground, and a fluorescence detector (FD) that measures the longitudinal development of the shower (Fig. 1.4).

The FD technique was pioneered by the Utah University group with the Fly's Eye detector, providing many important results, including the detection of the highest energy (3×10^{20}eV) cosmic ray measured so far [5,12].

Two main candidates were considered as surface detectors for the Auger Observatory: plastic scintillators and water Cherenkov counters. Both had been used efficiently in previous air shower experiments. They behave differently. Scintillators respond to all charged particles in proportion to their energy loss in the medium. The number of photons produced by a minimum ionizing particle is of the order 20 000 photons/cm in comparison with some 200 photons/cm in a water Cherenkov counter. For a slower particle, the scintillation yield increases in inverse proportion to energy while the Cherenkov yield decreases and even cancels for *β<1/n* (*n* being the refraction index of the radiator, 1.33 for water). However, in the case of electrons, which are very light particles, one needs to reach very low momenta, below 1MeV/c or so, before seeing such effects. Moreover, a major difference between scintillators and Cherenkov counters is the ability of the latter to convert nearly all photons as the radiation length is of the order of 40 cm in both materials: a typical scintillator radiator is a few percent of a radiation length thick while a typical Cherenkov radiator is several radiation lengths thick. Indeed, as scintillators are expensive (the mixing of the scintillating material in the plastic support and the optical quality of the surface require much care) they are usually made in the form of relatively thin plates (a few centimeters) that offer a cross-section to the shower that is strongly dependent on zenith angle (*cosθ*). The water Cherenkov detectors are much cheaper and can have instead a shape having similar dimensions in height and lateral extension, thereby offering to the shower a cross-section that is nearly independent on zenith angle. In practice a water depth of a meter or so is easy to implement and gives as much light as a one centimeter thick scintillator plate in the case of a minimum ionizing particle. Cherenkov counters, which were finally selected for the Auger surface detector for their lower price and good performance, are therefore very efficient detectors of soft electromagnetic showers which make up a large fraction of their signal.

The SD includes 1600 water Cherenkov tanks covering an area of 3000 km^2, and the FD includes four eyes each made of six different fluorescence detectors (Fig. 1.5).
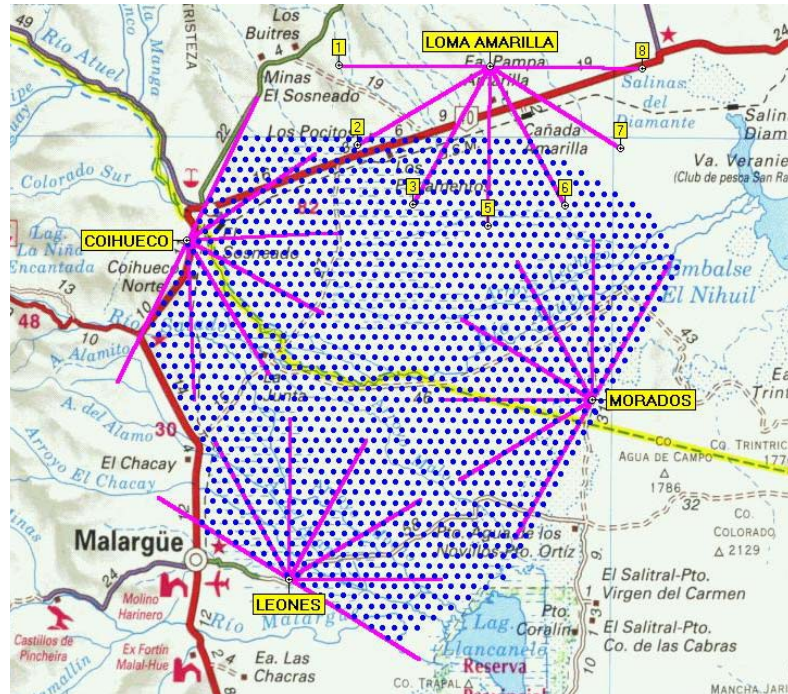
Figure 1.5 Map of the PAO southern site. Each dot represents the position of a Cherenkov tank. The array is viewed from four sides by fluorescent detectors.

The site is at an altitude of ~ 1400 m above sea level, corresponding to an atmospheric depth of some 875 g/cm^2, which corresponds to shower maximum for vertical showers in the energy range of interest. The construction of the observatory started in 1999 and is expected to be completed in 2006. By the end of 2005, more than 800 fully instrumented water tanks and three FD had been installed and are in operation or being run in.

1.3.1 The surface detector array

The ground array is made of 1600 cylindrical water Cherenkov counters located on a triangular lattice having a mesh size of 1.5 km (closest distance between two counters). Each tank contains a volume of 1.2 m×10 m^2 of high purity water, enclosed in a highly diffusive plastic (Tyvek) liner. The Cherenkov light

produced by relativistic shower particles crossing the water is observed by three 9''
photomultiplier tubes through polyethylene windows on the top of the liner. Signals
from the PMTs (anode and amplified last dynode) are read out by electronics
equipping each tank separately and the data are transmitted by radio to the data
acquisition centre. Each station is powered by batteries connected to two solar
panels (Fig. 1.6). The absolute time of arrival of the shower front on ground is
obtained from the global positioning satellite (GPS). For a same shower, the
detailed time sequence is recorded in flash analog to digital converters (FADC's)
equipping both the anode and last dynode. A reasonably low threshold must be
used, well below the signal given by relativistic minimum ionizing particles (one
talks of a VEM as the reference charge corresponding to the signal given by a
relativistic vertical muon) [13]. Such a threshold implies a phototube single rate
much too high to allow for recording all signals. A selection is therefore made at the
level of each tank, using several trigger conditions such that the total event rate is
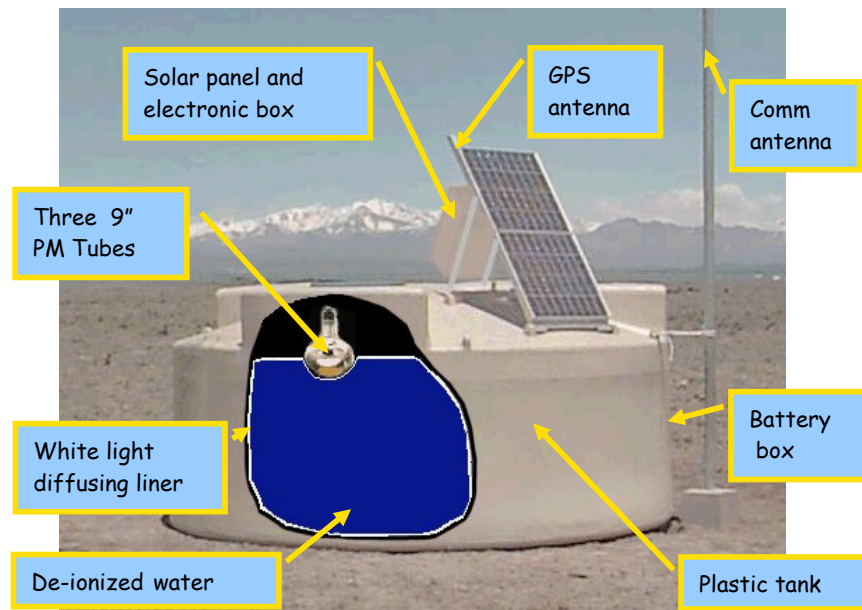kept at a reasonably low level.

Figure 1.6 Exploded view of an Auger Cherenkov tank.

The SD is designed to have a duty cycle of 100% over 20 years operation
independently from weather conditions.

The acceptance of the detector is such that, in the absence of a GZK cutoff, more than one shower having energy in excess of 10^{20} eV should be detected every month. Each such shower would typically involve 15 to 20 detectors. Its direction is obtained from the timing information (to a good approximation, the shower front is isochronous and sharp), its energy from the extension on ground of the area covered by the counters hit and from the amplitudes of their signals. A fit of the tank signals to a lateral distribution function that relates the signal amplitude S to r (its distance to the shower axis) and E (the shower energy) is made for each event. In Auger, the lateral distribution function is approximated by a form $S(r[km])=S(1000)\ r^{-v}$ with $v=\ 4.8-1.26\ sec\theta$ and the shower energy is inferred from the relation $E(EeV)=0.12(\sqrt{\{1+11.8(sec\theta\ -1)^2\}}\ S(1000))^{1.05}$ [7]. The angular and energy resolutions of the ground array have been estimated from simulations of the detector to be $\pm\ 1.5°$ and $\pm\ 20\%$ respectively.

1.3.2 The fluorescence detector

The fluorescence detector consists of four stations of six eyes each (Fig. 1.7). It measures the fluorescence radiation produced by the (highly collimated) shower particles on nitrogen molecules (near UV, $\sim$ 400 nm). It can only operate in clear moonless nights, implying a 10% duty cycle. The stations are located on the
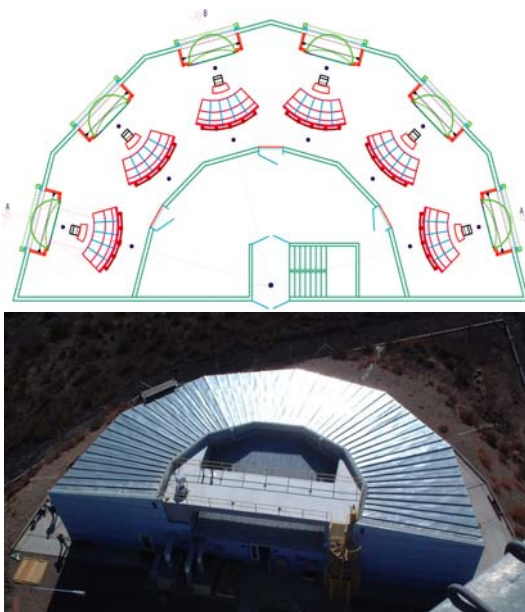

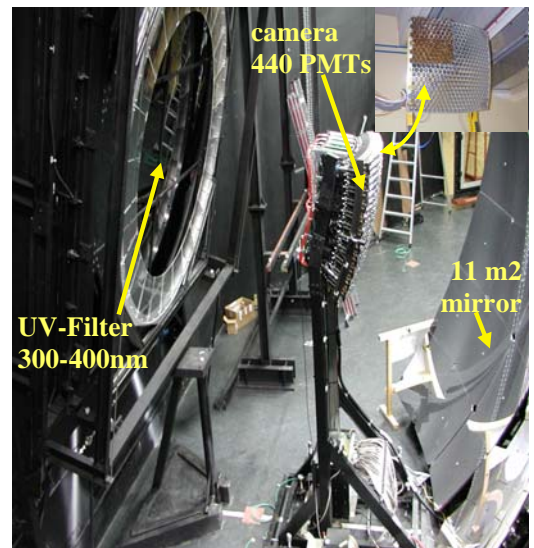Figure 1.7 A fluorescence station: schematic view (on top) and its photograph.

Figure 1.8 Photograph of an eye.

9

periphery of the SD area, nearly equidistant from each other, in such a way that any shower recorded in the SD is also observed in at least one of the eyes. Each eye covers a field of view of 30° in azimuth × 28° in elevation. It is equipped with a mirror focusing the light on an array of 22×20 pixels (photomultiplier tubes), each having 1.4° aperture. A UV filter and a diaphragm protect the detector assembly.

Figure 1.8 shows the photograph of an eye. It displays the large UV filter on the left, the array of photomultiplier pixels in the center and the focusing mirror on the right.

The amount of fluorescence light emitted is proportional to the number of charged particles in the shower, allowing for a direct measurement of the longitudinal shower profile, namely of the shower energy, and for the determination of the depth of shower maximum – X_{max}.

Monocular observation is insufficient for an accurate localization of the shower axis: a precise measurement requires binocular observation or, even better, hybrid detection as provided in the PAO. Indeed the observation of hybrid events, namely of events that are observed by both the FD and the SD simultaneously, is an essential asset of the PAO [8]. The systematic errors affecting the energy measurement in these detectors are of a very different nature and are essentially uncorrelated.

The fluorescence detector provides a direct measurement of the shower energy but its precise evaluation is made difficult [14] by a number of complications: imprecise knowledge of the fluorescence yield, light absorption in the atmosphere, contamination of Cherenkov light from the top of the atmosphere. On the contrary, the measurement of the particle density on ground in the surface detector is relatively easier but provides a very indirect measurement of the shower energy via its lateral distribution: it relies heavily on simulations and may suffer of systematic sources of uncertainties that are difficult to evaluate precisely and reliably.

Chapter 2 - THE VATLY DETECTOR

In order to acquire some familiarity with the behavior and performance of the Auger surface detector, a replica of one of its Cherenkov tanks has been constructed and installed on the roof of the VATLY laboratory (located at INST, Hanoi). Its response to muons has been studied using a trigger provided by a scintillator hodoscope located below it (Fig. 2.1). As an illustration of the performance of the hodoscope we describe, at the end of the present chapter, a search for atmospheric muons stopping into it.
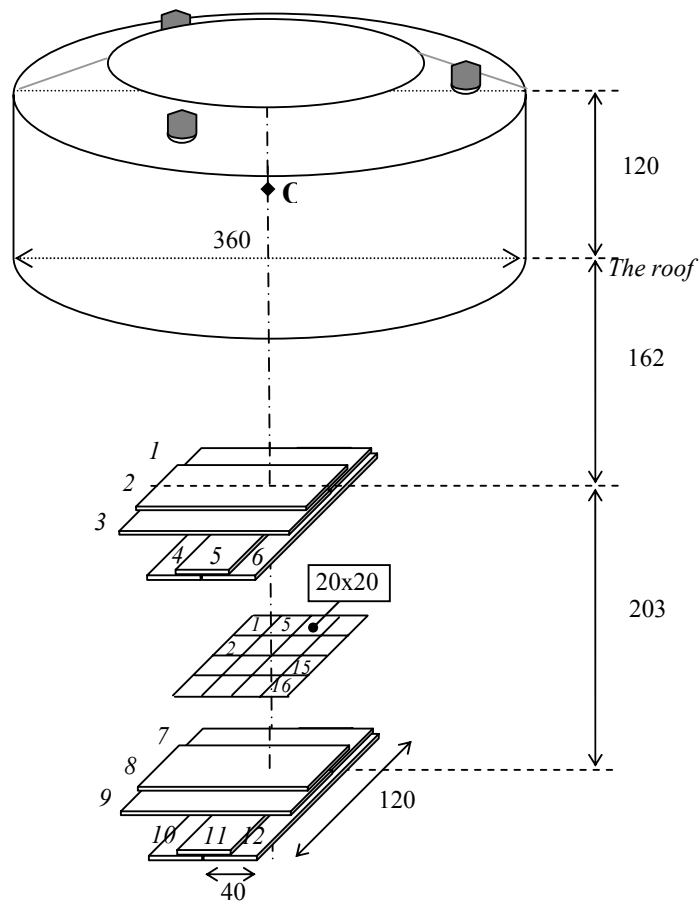
Figure 2.1. Schematic drawing of the setup (distances in centimeters).

2.1 The water Cherenkov counter

The Hanoi Cherenkov counter is made of a cylindrical water volume used as a radiator and a set of three photomultiplier tubes that collect the Cherenkov light.

The water volume is 3.6 m in diameter and 1.2 m in height. It is contained in a light-proof stainless steel tank. The water is taken from the town supply and filtered in two successive filters, eliminating particles having a diameter exceeding 10μm and 5μm respectively. The inner tank walls are painted white[2] to diffuse the Cherenkov light. Three 8'' photomultiplier tubes are installed on the top of the tank looking downward and collecting the Cherenkov light diffused on the tank walls. Each tube has eleven dynodes and two focusing electrodes. They are at a distance of 125cm from the tank vertical axis on radii separated by 120° from each other. Their spherical photocathodes are immersed in water and grounded to avoid microsparking across the glass envelope. Hence, the anode is biased with a positive high voltage, its signal being read out via a 50 Ω coaxial cable through a 10000 pF capacitor.

A relativistic particle vertically incident on the center of the counter produces ~ 200 detectable photons per cm, namely 24000 in total on Cherenkov cones having a half-aperture of $\theta_c=arccos(1/n) \sim 41^{o}$ [3]. The area of a photocathode is ~ 400 cm^2 while the area of the tank inner walls is 34 m^2, their ratio being $\rho=0.12\%$. In practice, the loss rate per diffusion is far from being negligible. However, if no light were lost in the tank walls and in the water, all the light would ultimately be collected by the tubes and, in the crude approximation of complete randomization, it would take some $1/\rho=800$ diffusions to reach that stage. In between successive diffusions the light travels at least 2.4m, significantly more when the light path is inclined with respect to the vertical, say 3 to 4m. The light velocity in water is 30/n cm/ns = 22cm/ns and the time between successive diffusions is therefore of the order of 15ns. In the ideal case the light signal would therefore last some 10μs. This is very far from reality. In the case of the Auger tanks, which are filled with water of extreme purity and coated with a white plastic sheet of very high diffusivity (the Tyvek bag), the pulse duration is typically 100 ns (it has a sharp rise time and falls exponentially with 70ns decay time) and the effective number of diffusions is of the order of 6. In such a case the amount of light collected by a tube cannot exceed $6\rho =0.7\%$. It will in fact be less because a

---

[2] Lobster paint from Urai Phanich.
[3] Here n is the index of refraction of water. The number of Cherenkov photons per unit path length is given by $dN/dx=2\pi\alpha z^2 sin^2\theta_c(\lambda_2-\lambda_1)/\lambda_2\lambda_1$, where α is the fine structure constant, z is the electric charge of the particle, λ_2 and λ_1 are the limits of integration on the photon wavelength. Here we calculated for singly charged particles (z=1) and the emitted light wavelengths in the range from UV to visible (where glass and water are transparent).

significant amount of light is absorbed in the water and in the walls. A precise evaluation of this number knowing the light attenuation in water and its absorption in the walls implies a detailed simulation that is well beyond the scope of the present rough estimate. However, we can estimate how many photoelectrons, n_{pe}, have been collected by one tube from the relative width of the VEM signal, $\Delta S/S = 1/\sqrt{n_{pe}}$. In Auger, this number is of the order of 26% (15% for three PMT's), corresponding to 15 photoelectrons per PMT, 45 in total [15]. From the resolution achieved in the VATLY tank we shall be able to estimate this way the number of photoelectrons collected and the relative deterioration of the water quality and of the tank diffusivity. Note that in Auger, the photocathode efficiency is as high as can be routinely achieved, of the order of 20%. However, a lower value, of the order of 10%, should be expected for the old VATLY tubes.

2.2 The scintillator hodoscope

The scintillator hodoscope [16] consists of two sets of scintillator plates. Each set, separated from the other by 2m, consists of six plates arranged in four layers, each 3 cm thick (Fig. 2.1). The odd layers (layers are numbered from top to bottom) are made of one $120 \times 40 \text{cm}^2$ scintillator plate and the even layers are made of two plates of $80 \times 40 \text{cm}^2$ scintillator glued to a $40 \times 40 \text{cm}^2$ lucite plate. Each plate is viewed by a 2'' photomultiplier tube via a 15 cm long cylindrical lucite light guide glued on the narrow plate side (in the case of the odd layer, on the lucite light guides glued on the lucite plates). The scintillator plates are arranged in such a way as to allow for an effective segmentation into 16 squares of $20 \times 20 \text{cm}^2$. The lower set can be moved around in order to vary the mean incidence angle accepted by the hodoscope.

2.3 Electronics

Each PMT signal was resistively split in two equal parts, one being analyzed in an analog to digital converter (ADC – LRS 2249A, 0.25pC per channel) and the other used to feed a discriminator having an input threshold of 10mV and giving output NIM signals of 40ns width, one of which is sent to a time to digital converter (TDC – LRS 2228, 0.5ns per channel) (Fig. 2.2). The discriminator signals of the hodoscope PMT's are also used to produce a trigger using the even layers exclusively (each layer signal being obtained by ORing the signals of the two plates in the layer). A trigger on through going muons requires a fourfold coincidence

between the four layers while a trigger on stopping muons requires only a threefold coincidence between the three uppermost layers. The final trigger pulse is broadened to 100 ns in order to provide a gate for the analog to digital converters. It is also used to start the time to digital converters.
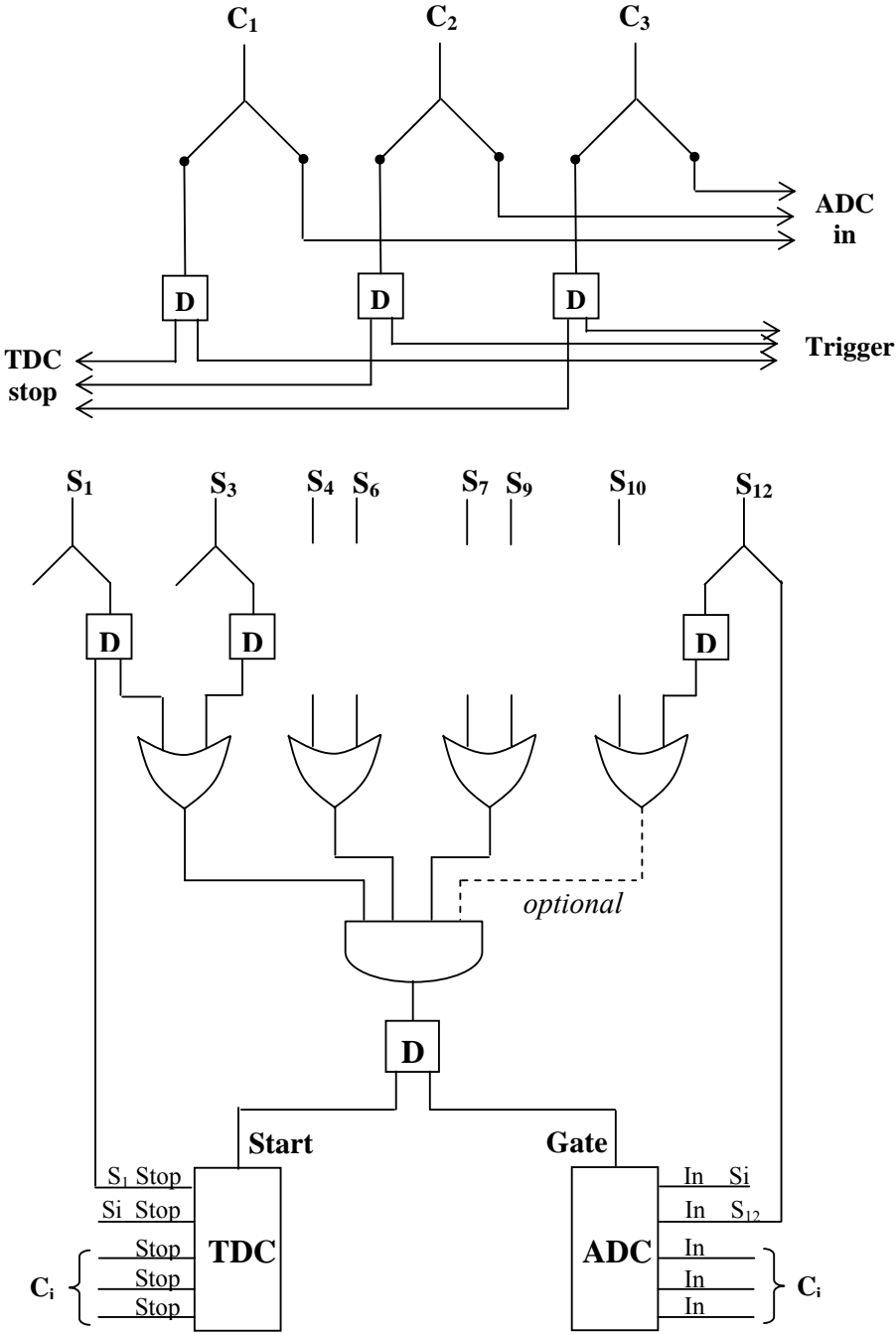

Figure 2.2: Schematic diagram of the electronics

2.4 Observing muons stopping in the scintillator hodoscope

As an illustration of the good performance of our scintillator hodoscope we have searched for a signal of muons stopping in it, a rather rare event. Stopping muons can be recognized from three different features: the absence of signal in the layer(s) following the place where the muon stopped, a longer time of flight between the upper and lower layers (because of the lower momentum), a Bragg-like signal distribution in the layers preceding the place where the muon stops. This naturally leads to look for muons stopping in the lower layer, the three upper layers being used to define a good geometry, to provide a time of flight measurement and to measure accurately the Bragg curve. Therefore, data were taken by requiring a coincidence between the three upper even layers (the normal trigger requiring a coincidence between all four even layers, see Fig. 2.1 and 2.2).

2.4.1 Criteria used for the selection of stopping muons

We must select a sample of muon candidates such that we can make an efficient use of the above features. Several considerations are relevant to this choice:

– Signals in both even and odd layers are necessary in order to have as good as possible a measurement of the Bragg curve. This restricts the useful detector area to the central square, 40×40 cm^2.

– Indeed, having a signal in each of the four upper layers restricts the muon impact to be within this 40×40 cm^2 square but the angle of incidence may still be quite large. In order to have the impact on the lower layers similarly restricted to the 40×40 cm^2 central square, we need a signal in both the 5th and 7th layers. This, however, leaves only the 8th (and last) layer in which to require the absence of a signal.

– In order to minimize the contamination by electrons or other non‑muon components, we reject events containing multiple tracks, which can be done by asking to have one and only one scintillator hit in each of layers 2, 4 and 6.

Accordingly, the basic data sample consists of:

– Data sample collected on the 13th of March 2005, containing 1.1 x10^6 trigger events (coincidence between the three upper layers),

– Require 1 and only 1 "on" counter in each of the 7 first layers ("on" means pulse height > 20 channels, namely > 0.1 *mip* [4], its timing with respect to the trigger being within a 15 ns window, 21866 events pass this selection.

– Of these, 656 have less than 0.1mip in the 8th (last) layer and are retained as stopping muon candidates. On the contrary those that go through will be used to provide a reference sample of through going muons.

2.4.2 What do we expect?

Figure 2.3 shows the shape of the Bragg curve that we have calculated from the Bethe-Bloch relation with an ionization potential of 10 eV and neglecting the field effect. Normalization is made at minimum, using the value of 1.8 MeV/(g/cm^2) [17].

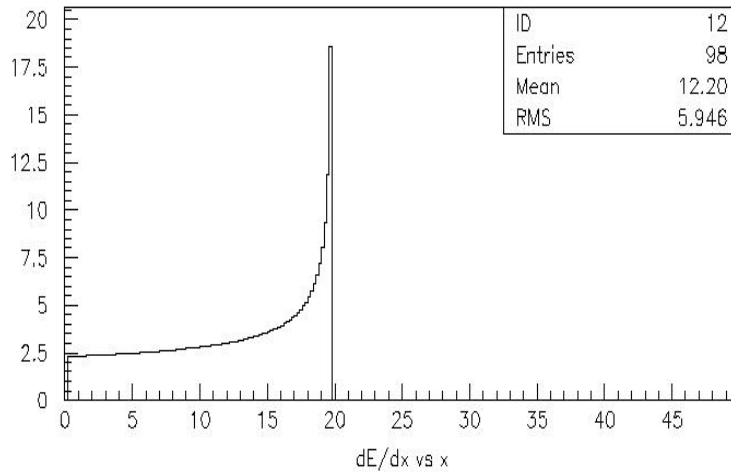Figure 2.3: Bragg curve for *p*=138 MeV/c incident muons. The energy loss/(g/cm^2), measured in MeV, is shown as a function of the thickness traversed (in g/cm^2).

As we require a signal in the 7th layer, we consider muons stopping in that layer (i.e. we use layers 1 to 6 for the Bragg curve and for the time of flight, layer 8 for the absence of signal). Muons, stopping at the very beginning (end) of layer 7, have a momentum of 133 (142) MeV/c. We do not attempt to distinguish between muons stopping at different depths in layer 7, therefore we take a reference Bragg curve (for stopping muons) evaluated as the average between the above two extreme curves and calculate associated uncertainties accordingly. Note that our reference

---

[4] 1mip is defined as the area (charge) of the pulse created by a minimum ionizing particle in the scintillator.

Bragg curve differs slightly from the Bragg curve associated with the average momentum (138 MeV/c). Table 2.1 lists the results obtained for four different incident momenta, 133, 138, 142 and 4800 MeV/c. The last one corresponds to the mean muon momentum, with a nearly constant energy loss. It is used to define our *mip* reference. The entries in the columns labeled E_i are energy losses in layer *i* measured in MeV and the last column is the time of flight between the upper and lower layers measured in ns.

Table 2.1

P (MeV/c)	E1	E2	E3	E4	E5	E6	E7	ToF
133	7.23	7.65	8.26	9.24	11.21	24.83	-	10.4
138	7.05	7.40	7.88	8.62	9.90	13.03	14.67	9.9
142	6.92	7.22	7.64	8.24	9.20	11.12	21.44	9.6
4800	6.86	6.86	6.86	6.86	6.86	6.85	6.85	6.7

The momentum window in which we expect muons to stop in layer 7 is at most 9 MeV/c. Taking as a rough approximation that half of the muons have a momentum lower than 4800 MeV/c and that their spectrum is flat in this region, we expect a fraction < ½ 9/4800 = 0.09% of the muons to stop. As we have 21866 muons to start with, this means that the expected size of the final sample (an order of magnitude estimate) should be of the order of 20 events (more because a flat spectrum is a pessimistic assumption, but less because the efficiency of our selection will not be perfect).

2.4.3 Selecting stopping muons.

We first use a reference sample of muons crossing the eight layers by requiring one and only one counter "on" in the 8th layer (there are 19461 such events). In a first step, all ADC pulse heights are normalized to *mip'*s and all TDC times (measuring the time at which a pulse arrives with respect to the trigger pulse) are shifted to zero on average by using proper parameters for each individual counter. These TDC times are then corrected for two effects: time taken by light to transit inside the scintillator and time slewing (these corrections are zero on average). The first correction can only be applied to the upper layers in the case of stopping muons (as we are not using layers 7 and 8) but it can be used on both

upper and lower layers in the present reference sample. It amounts to 0.03ns/cm. The time slew correction is calculated by fitting a common slew parameter to all 8 layers in the reference sample and is found to be 1.5ns/*mip*.

We calculate the χ^2 distribution of the reference sample to the 4800 MeV/c Bragg curve, $\left.\chi^2_{thru}\right|_j = \sum_{i=1}^{8}\left(s_{ji}/\bar{s}_i - 1\right)^2 / \left(\Delta s_i\right)^2$, where j labels the event and $\bar{s}_i$ and $\bar{s}_i\Delta s_i$ are respectively the mean and *rms* values of the pulse height s_{ji} distribution in layer *i*. It is shown in Figure 2.4. Its mean value is 9.2 for 8 degrees of freedom and *rms*/mean =1.2, in agreement with expectation.

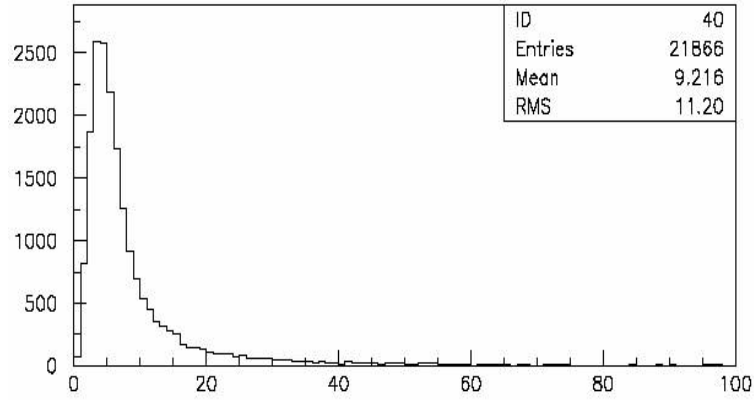| ID | 40 |
Entries	21866
Mean	9.216
RMS	11.20

Figure 2.4: χ^2_{thru} distribution for the reference sample of crossing muons.

Selecting events with $\chi^2_{thru} < 10$ (14728 events), we show in Figures 2.5 and 2.6 their pulse height distribution (averaged over the 8 layers) and their time of flight distribution. The time of flight is defined here as $\Delta t = t_{down} - t_{up} = \sum_{k=5}^{8} t_k/4 - \sum_{k=1}^{4} t_k/4$, where t_k is the time of arrival of the signal recorded in the kth layer minus its average value in that layer. This means that Δt is zero on average: it is the difference between the actual time of flight and its average value of 6.7ns corresponding to relativistic particles. The quality of the data is a check of the correctness of the procedure. In order to measure the time of flight resolution that can be expected in the selection of stopped muons, the time of flight must be redefined by using layers 1 to 6 exclusively (layers 7 and 8 are not available in the stopped muon sample), implying that we do not correct the lower layer times for the impact to PMT distance. The result is shown in Figure 2.6 as a dotted line.
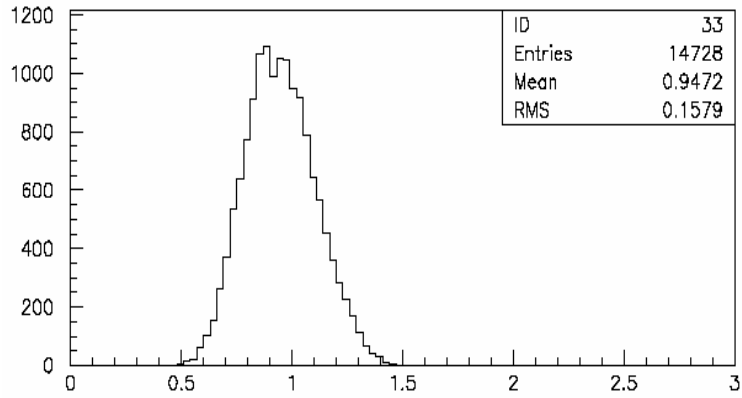
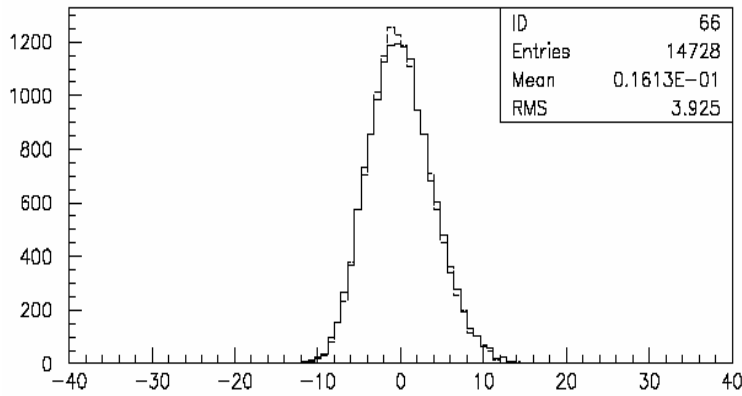Figure 2.5: Average pulse height (*mip*) distribution of events having χ^2_{thru} <10.

Figure 2.6: Time of flight distribution of events having χ^2_{thru} <10 calculated using all counters (full line) or layers 1 to 6 only (dotted line).

We now select stopping muon candidates by requiring the total pulse height in the 8th layer not to exceed 0.1mip (656 events). The distribution of their χ^2 to the stopping muon Bragg curve, χ^2_{stop}, is shown in Figure 2.7. It is compared with that of the 14728 through going muons (scaled by a factor 656/14728, dotted line). Their time of flight distribution is shown in Figure 2.8, again compared with that of through going muons as in Figure 2.7.

Recalling that what we call "time of flight" here is in fact the real time of flight decreased by 6.7 ns, we see from Table 2.1 that stopping muons are expected to have a "time of flight" of 9.9–6.7=3.2 ns.
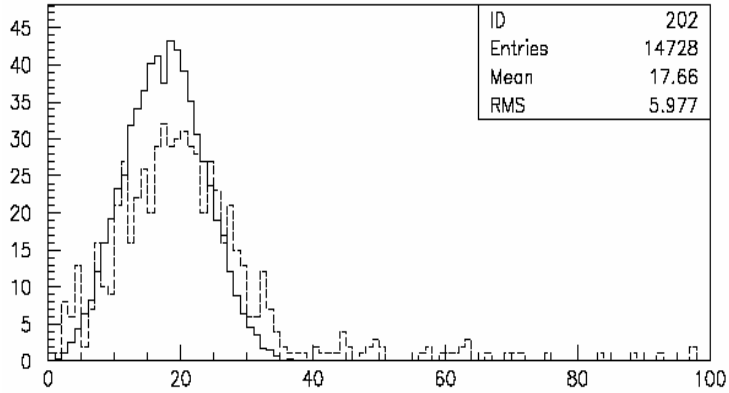
Figure 2.7. χ^2_{stop} distribution of the 656 stopping muon candidates (dotted line) as compared with that of the reference sample of through going muons (full line). The very small excess at χ^2_{stop} <10 is the possible signal we are looking for.
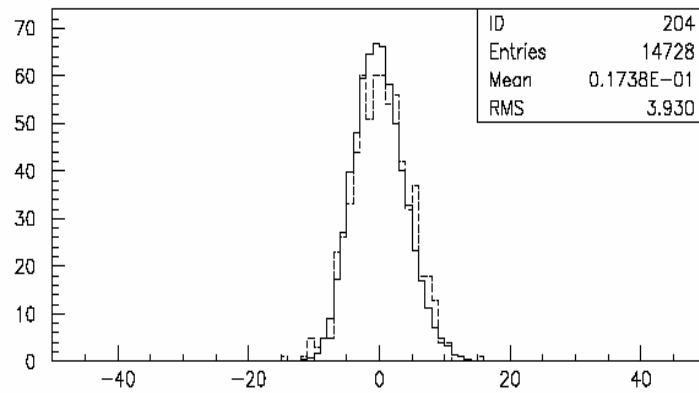

Figure 2.8. Time of flight distribution of the 656 stopping muon candidates (dotted line) as compared with that of the reference sample of through going muons (full line). A possible excess at large time of flights is what we are looking for.

In both Figures 2.7 and 2.8 there is still no clear signal to be seen (we are looking for an excess of events at low χ^2_{stop} and large times of flight). Next we retain only events having χ^2_{stop} <10 and compare the time of flight distributions of the two samples in Figure 2.9. Here we normalize the two curves in the region of negative time of flights where the contamination of stopped muons is expected to be negligible. A possible signal is now visible, but we need to evaluate its significance.
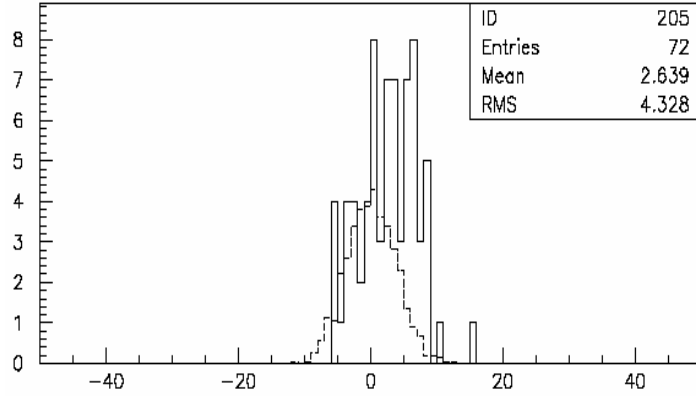
Figure 2.9: Time of flight distribution of stopping muon candidates having χ^2_{stop}<10 (full line) as compared with that of the through going muons(reference sample), having also χ^2_{stop}<10 (dotted line). Normalization is made in the region of negative time of flights.

We have 72 stopping muon candidates having χ^2_{stop} <10, of which 19 have a negative time of flight and 53 have a positive time of flight. We have 1569 through going muons having χ^2_{stop} <10, of which 767 have a negative time of flight and 802 have a positive time of flight. The possible signal is therefore 53-802×19/767=33.1 events with an uncertainty of $\sqrt{(53+19\times[802/767]^2)}$ = 8.6. We therefore have a signal at a level of 33.1/8.6 = 3.8 standard deviations. Note that if we accept that the final stopping muon candidates sample consists of 33 stopping muons and 39 non stopping muons, we would expect the mean time of flight to be 33×3.2/72=1.5 ns (the average time of flight of through going muons is 0 by construction and 3.2ns is taken from from Table 2.1 as the time of flight difference between the 138MeV/c and 4800 MeV/c samples). In fact, the mean time of flight of the final 72 events sample is 2.6 channels, namely 1.3 ns compared to the 1.5 ns expected. This good agreement gives us confidence on the reality of the observed signal.

We can therefore conclude that we have found evidence for a 3.8 standard deviation signal of 33 stopping muons, in good qualitative agreement with expectation. This result is an illustration of the good performance of our hodoscope. However, the very low size of the sample, obtained from over one million triggers, and its lack of purity, preclude the use of this method as a way to study muon decays.

Chapter 3 - RESPONSE OF THE VATLY CHERENKOV COUNTER
TO ATMOSPHERIC MUONS

3.1 Experimental arrangement

The response of the VATLY Cherenkov counter has been studied using atmospheric muons as a probe. The hodoscope system described in the previous chapter was used to select such muons. For a muon to give a trigger in the scintillator hodoscope (~ 25 g/cm^2) it must have at least 160 MeV/c when entering it. This corresponds to a β of 0.83 and this muon is therefore essentially relativistic. Taking into account the water Cherenkov counter (~ 120g/cm^2) and the roof of the laboratory (~ 45g/cm^2) the muon must therefore have at least 500MeV/c when entering the Cherenkov tank. This is much lower than the average muon momentum (4800MeV/c), implying that most crossing muons are highly relativistic. The hodoscope allows for the definition of 16×16 = 256 different "beams" having a typical cross-section of 1600 cm^2 in the medium plane of the Cherenkov counter (see Figure 3.1). Moreover, the lower hodoscope counters can be moved around in order to vary the average incidence direction. In practice three different geometries have been used: central (vertical incidence), west and north (average zenith angles of $\sim 30^o$). The hodoscope coincidence was used as a trigger and to open the ADC 100ns gate and start the TDC's.
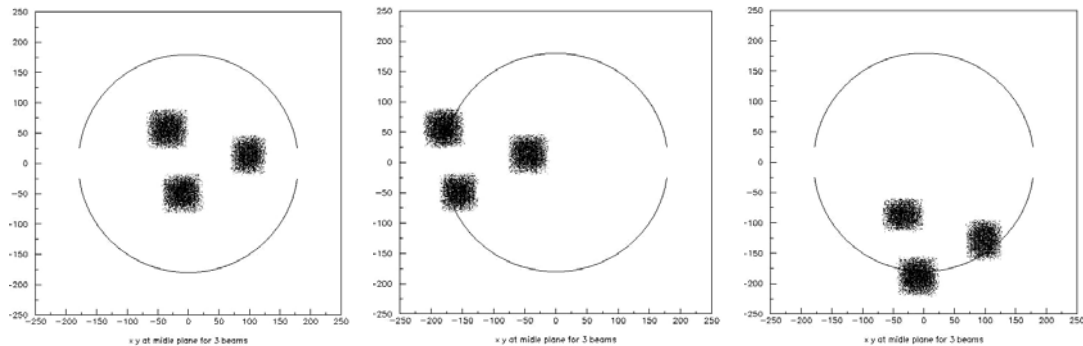

Figure 3.1: Impacts of three of the 256 possible "beams" on the middle plane of the counter for the central, west and respectively north geometries (from left to right).

3.2 Event selection

In all what follows, we only consider "good muons" defined as having an

average hodoscope pulse height between 0.6 and 1.5 *mip* and an average hodoscope time of flight between 0 and 12 ns (the average being made over the hodoscope layers).

Typical (central geometry) Cherenkov time distributions and pulse area spectra are shown in Figures 3.2 and 3.3 respectively. Typically 10.5% of the entries in the time distributions overflow the TDC. The reason is that their pulse heights are too low to trigger the discriminator that stops the TDC. The distributions of the others have a width of the order of $\pm$ 7 ns, as expected from the geometry of the light collection and of the PMT itself. A few low pulses, yet above discriminator threshold, give a high time tail. Pulse height distributions are very wide and extend to zero without decreasing. This is a disappointing result as all events of the central
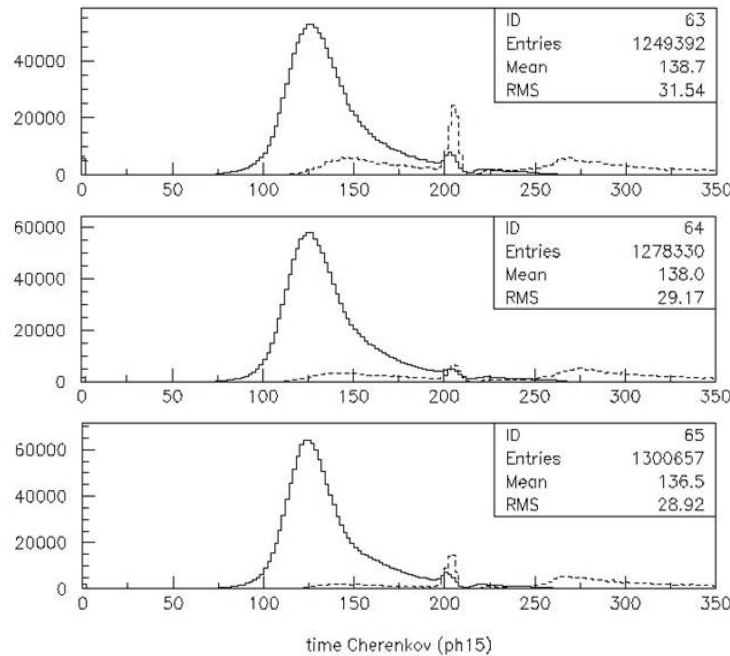
Figure 3.2: Time distributions of "very lows" (dashed line) and the complementary samples (full line). Most of the "very lows" overflow the TDC (at 4094) and are outside the figure. Only a small fraction is inside, it has been multiplied by a factor 10 in order to make it visible.

geometry sample are associated with a long (typically 120cm) track length in water: one would expect them to give a much narrower signal. We define a "very low" pulse height as having less than 15 ADC counts and a "very late" signal as having more than 190 TDC counts (late with respect to the trigger). The small bump

around channel 200 in Figure 3.2 was identified as due to cross-talk between the ADC NIM gate and the ADC input: when the ADC gate opens (which happens at a well defined time with respect to the TDC start) a small cross-talk appears on the ADC input and feeds into the TDC discriminator and the TDC stop (through the passive splitter), therefore reaching the TDC stop at a fixed time after the TDC start.
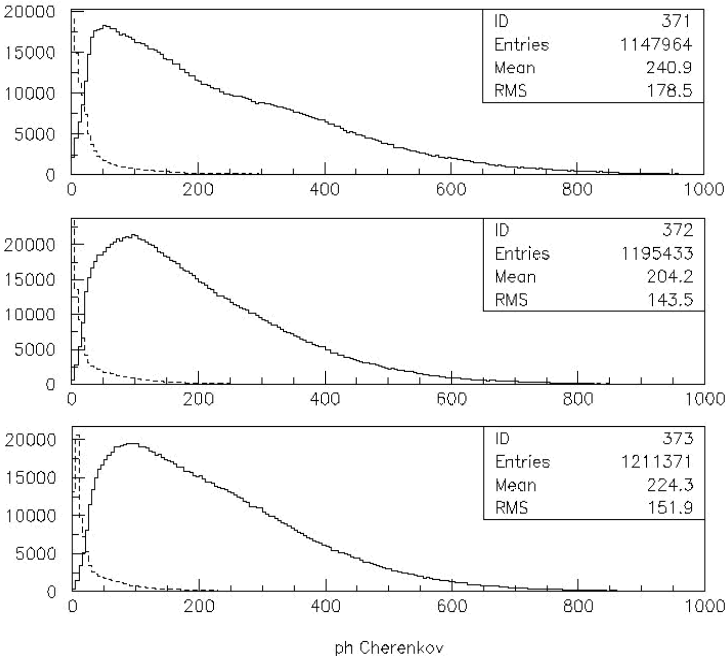
Figure 3.3: Pulse area distributions for "very lates" (dashed line) and the complementary samples (full line). The "very lates" have been divided by a factor 2 for convenience.

Figure 3.3 gives evidence for the presence of very low pulse heights that are usually associated with high times (or even overflows). The distribution of the fractions of pulse heights lower than 10 ADC counts is as follows:

Table 3.1

Number of very lows	Fraction of events (total $1.44 \ 10^6$ events)	Uncorrelated fractions (11.3%)
0	0.697	0.697
1	0.267	0.267
2	0.032	0.034
3	0.004	0.001

24

From the table above we see that the probability to have a pulse lower than 10 ADC counts is 11.3% per PMT and that there is very little correlation between the three PMT's, namely having a very low pulse height is a property of the PMT and not of the event. One possible reason for having a low pulse height is that the track is far away from the PMT. To investigate this possibility we define for each PMT_i a distance d_i ; d_i is measured between the impact of the muon track on the lower Cherenkov plane ($z = -60$cm) and the vertical projection on that same plane of the centre of the PMT photocathode. One should be careful when cutting on d_i : they are strongly correlated as illustrated in the Appendix. Figure 3.4 shows the distribution of d_i for "very lows" (dashed line) and not "very lows" (full line). Figure 3.5 shows the distribution of d_i for "very lates" (dashed line) and not "very lates" (full line). The observed structure is due to the fact that for each PMT d_i can take only 256 different values. Figures 3.2 to 3.5 give evidence for a very strong correlation between "very lows" and "very lates", most of them associated with pulses that are below the threshold of the discriminator that feeds the TDC. The correlation with high values of d_i is significant but much smaller. There are many very low pulses that are not associated with a large d_i value. At this stage, it is not clear what they are due to.
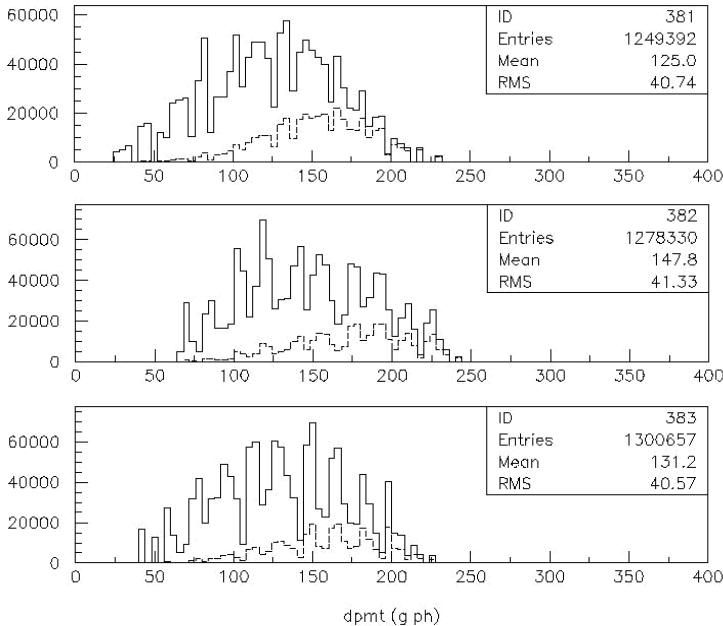

Figure 3.4: Distributions of d_i for "very lows" (dashed line, multiplied by 2 for convenience) and for the complementary samples (full line).
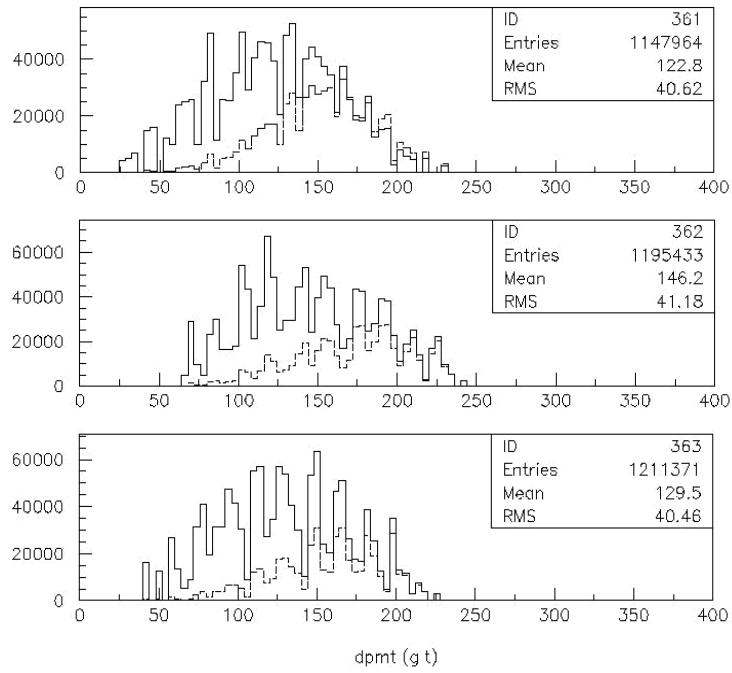
25

Figure 3.5: Distributions of d_i for "very lates"(dashed line, multiplied by 2 for convenience) and for the complementary samples (full line).
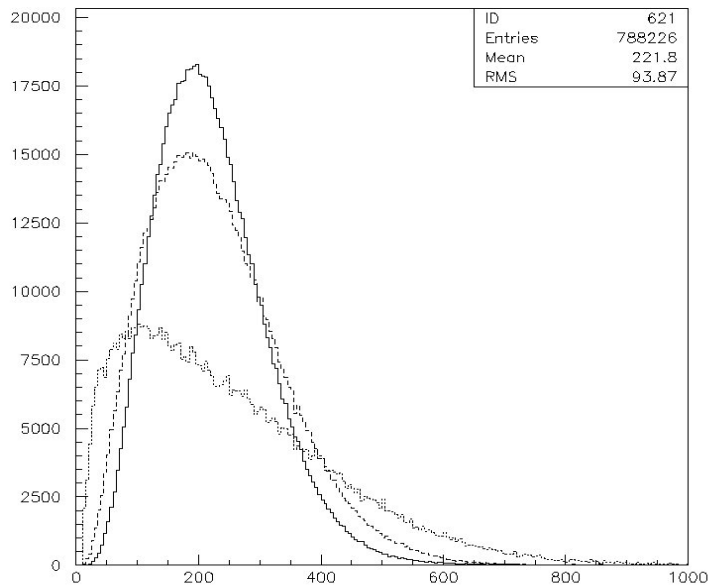

Figure 3.6: Pulse height distributions of events having 3 (full line), 2 (dashed line) and respectively 1 (dotted line) "good PMT's". The plotted pulse height is the average of the "good PMT's" pulse heights. The 2 (respectively 1) "good PMT's" data have been multiplied by 1.5 (respectively 6) for convenience.

26

From there on a "good PMT" is defined as having a TDC time less than 190 channels and a pulse height in excess of 10 ADC counts, namely as being neither a "very low" nor a "very late". Figure 3.6 shows the distributions of PMT pulse heights averaged over "good PMT's" for events having 3, 2, 1 and 0 "good PMT's" respectively.

The table below summarizes the results.

Table 3.2

Number of "good PMT's"	Number of events	*Rms*/mean (%)	$\sim n^{-1/2}$
3	788 226 (55%)	42	40
2	539 062 (37%)	48	49
1	104 815 (7%)	67	69
0	8 728 (1%)	-	-

This table gives confirmation of the relative independence of the PMT's with respect to each other. In fact it looks like the width is solely caused by the small amount of light collected in each PMT: the relative width of the pulse height distribution measured with n PMT's is nearly inversely proportional to $n^{1/2}$ as shown in the last column of the table. Events having no "good PMT" represent only 0.6% of the total event sample. Note that even in the case of 3 good PMT's we have *rms*/mean = 42% compared to 15% in Auger, suggesting that we have some 8 times less photoelectrons than in Auger.

3.3 Cherenkov spectra

We now consider only events having at least 2 "good PMT's" and of course being "good muons". The width of the pulse area distribution is the result of several effects: spread of the track length distribution, diffusion of the light on the counter walls, attenuation in the water, response of the phototubes. To a good approximation atmospheric muons can be considered relativistic ($<p>/m=4.8\text{GeV}/106\text{MeV} \sim 50$, correspond to $\beta \sim 0.999$) and the light yield to be constant and ~ 200 photons/cm. The pulse area ph_i of PMT i is parameterized in the form of $ph_i=\lambda_i l(1+\alpha_i(d_i-d_0))$ where l is the track length of the muon in water, d_0

an arbitrary average distance and d_i as defined above. The coefficients λ_i and α_i must be evaluated from the data. The λ_i's depend on the overall gain while the α_i's should depend mostly on the light attenuation in water, and therefore, to first order, be independent of i.

3.3.1 d - dependence

We first look at data taken in the central geometry. Most muons have a track length of 120cm in this case and no muon has a track length smaller than 118 cm.

The d_i distributions shown in Figure 3.5 have mean values of 129, 151 and 134 cm respectively, namely 138 cm on average. Figure 3.7 illustrates the dependence of ph_i on d_i for "good PMT's".

What is shown in fact is the dependence of $d'_i = d_0 + \{(ph_i/\lambda_i l)-1\}/\alpha_i$ on d_i. In order to evaluate this expression we used the values of λ and α that give the best fit to the expression used to describe ph and take $d_0 = 138$ cm, the average value of the d'_is. The data are binned in bins of 15 cm and the mean value of d'_i is plotted in each d_i bin. This figure gives evidence for a significant dependence of ph over d. It also shows that the expression used to parameterize ph is reasonable. However the flattening at high d values suggests cutting d at something like 180 cm.
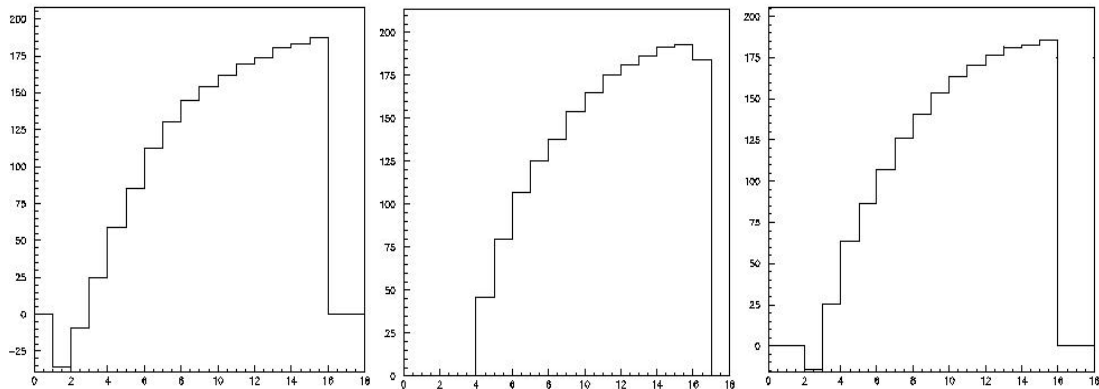

Figure 3.7: Dependence of d' on d for each of the three PMT's

We therefore repeat the analysis with such a d cut-off and calculate again the values of λ and α that give the best fit. The results are shown in the table below. The χ^2 was calculated using an uncertainty $\Delta ph=0.2\times ph+40$.

Table 3.3

I	1	2	3
λ	1.08	1.12	1.15
α (%)	-0.64	-0.55	-0.56
χ^2/dof	2.7	2.1	2.2
Rms/mean not corr (%)	73.7	70.2	67.7
Rms/mean corr (%)	71.1	68.0	65.3

The pulse height distributions of "good PMT's" are displayed in Figure 3.8 before and after correcting for the *d* dependence. The improvement is small but significant, as shown from the ratios between *rms* and mean listed in the table.
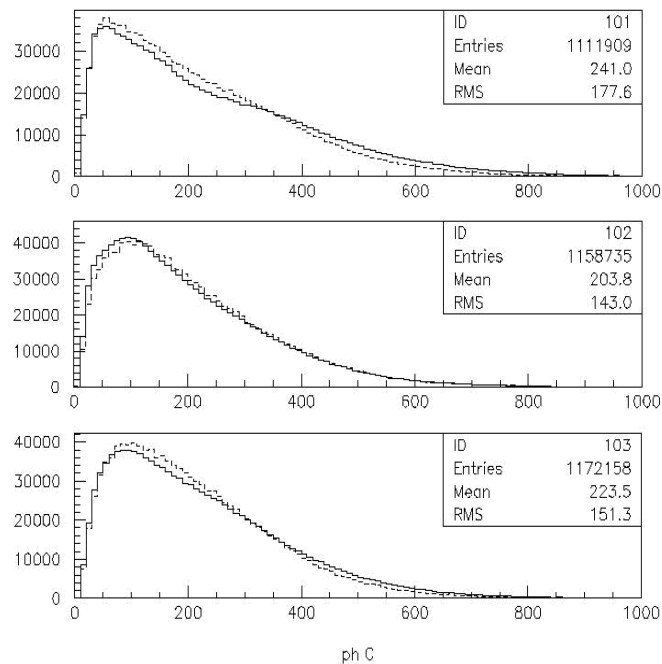

Figure 3.8: Pulse height distributions of "good PMT's" for "good muon" events having at least two "good PMT's". Full (dashed) lines are for uncorrected (*d*-corrected) data.

However, as illustrated on Figure 3.9, the improvement achieved on the average of the "good" pulse heights of a same event is negligible: the ratio *rms/*mean changes only from 44.9% to 44.8%. We note that the three values found for α are similar, − 0.58% on average, corresponding to an effective absorption
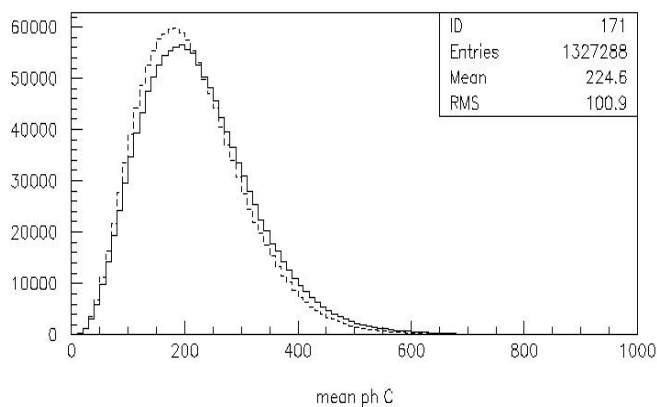
Figure 3.9: Pulse height distribution for *good muon* events having at least two *good PMT's* averaged over *good PMT's*. Full (dashed) line is for uncorrected (*d*-corrected) data.

length of 1.7 m. The absence of improvement observed on the mean pulse height implies that the *d*-corrections somehow compensate each other and are therefore unnecessary. Accordingly, in what follows, a fixed correction ($\alpha = -0.58\%$) is applied to each of the three PMTs. In the north and west geometries, we may expect somewhat different *d*-dependences but the effect is so small and so well taken care of by the simple averaging of the three pulse heights that we shall not worry about it any longer.

3.3.2 *l* - dependence

In order to study the *l*-dependence, we switch to the west and north data samples. Only events having *l* > 20 cm have been retained. However we now relax the requirements about "good PMT's": namely we accept all "good muons" and include all PMT's. Otherwise we would unduly bias our sample. Indeed, for low *l* values, there is a very high probability to have "bad PMT's". This is illustrated in Figure 3.10 which shows *l* distributions for events having 0, 1, 2 and 3 "good PMT's" respectively.

A clear correlation is visible, indicating that low track lengths are preferentially associated with bad PMT's. A better way to see that is to look at the evolution of the pulse height distributions with increasing track length. This is done in Figure 3.11, the quantity plotted being the average of the three PMT pulse heights. This figure shows the increase of average pulse height as a function of track length, but,

30

at the same time, it also shows that the PMT gains are too low for small track length events (remember that the PMT signals are not amplified here, while in Auger they are); the pulse height spectra are cut at low values. The relative widths (*rms*/mean) are shown in Figure 3.12.
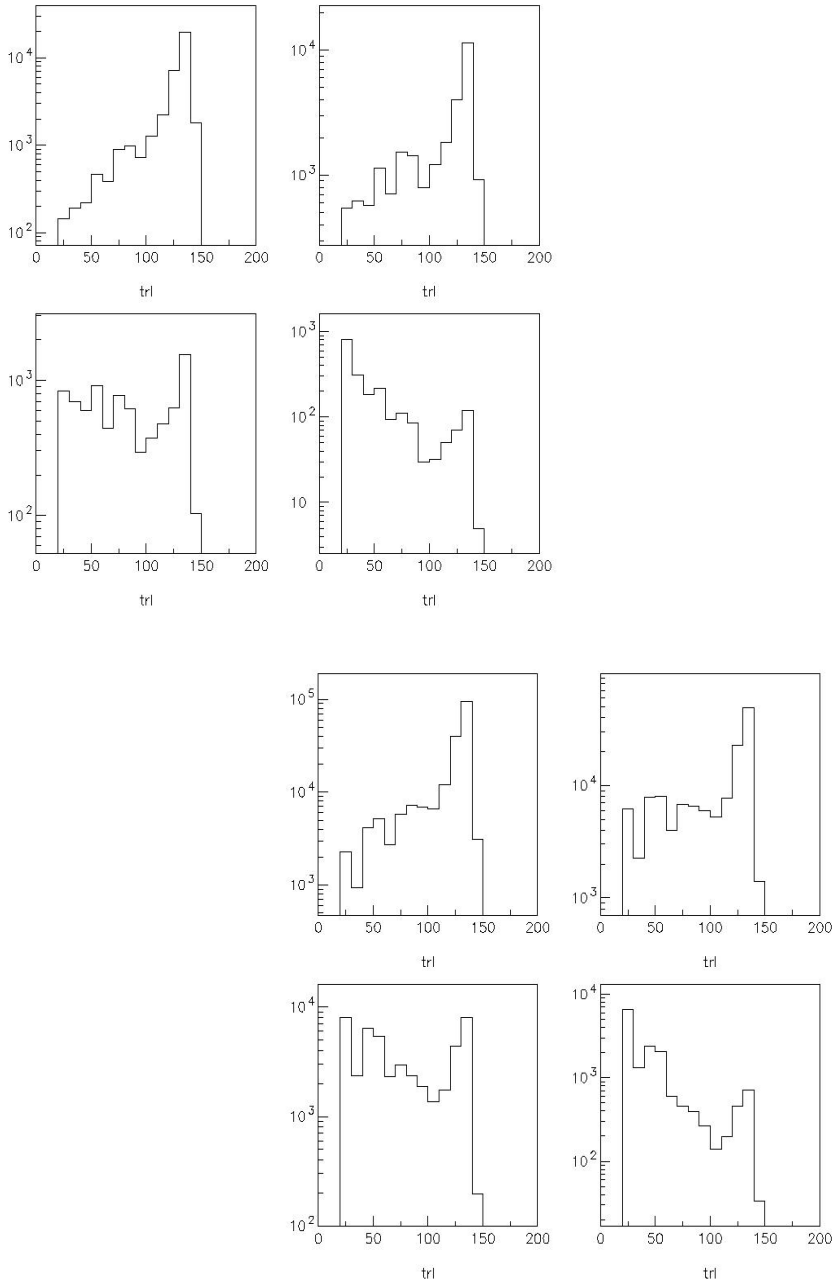

Figure 3.10: Track length distributions for good muons having 3, 2, 1 and 0 good PMT's (from left to right, top to bottom). West and north data are shown in sequence.
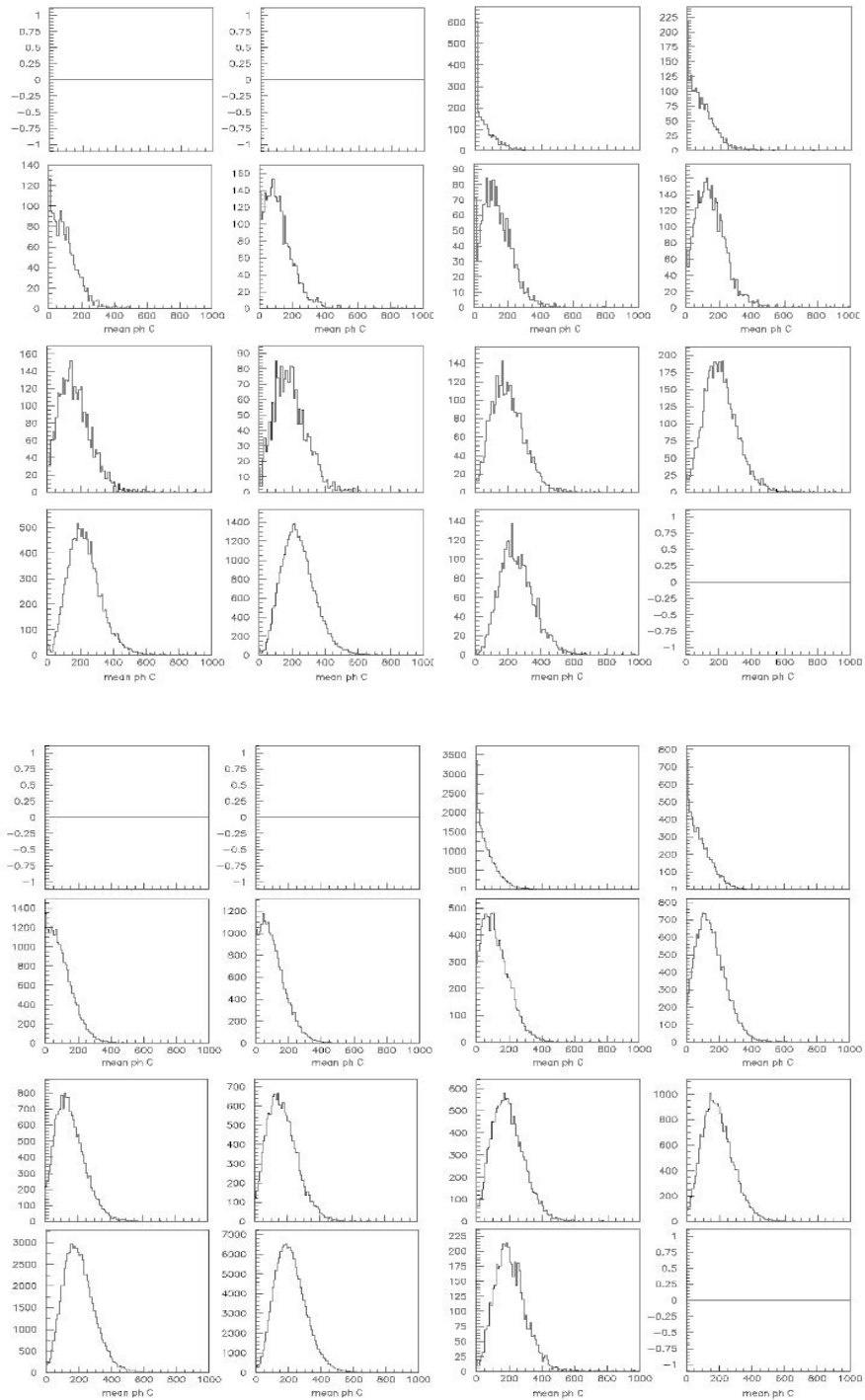
Figure 3.11: Pulse height distributions of good muons averaged over the three PMTs.
Each curve is for a given 10 cm wide track length bin, from 0 to 10 up to 150 to 160.
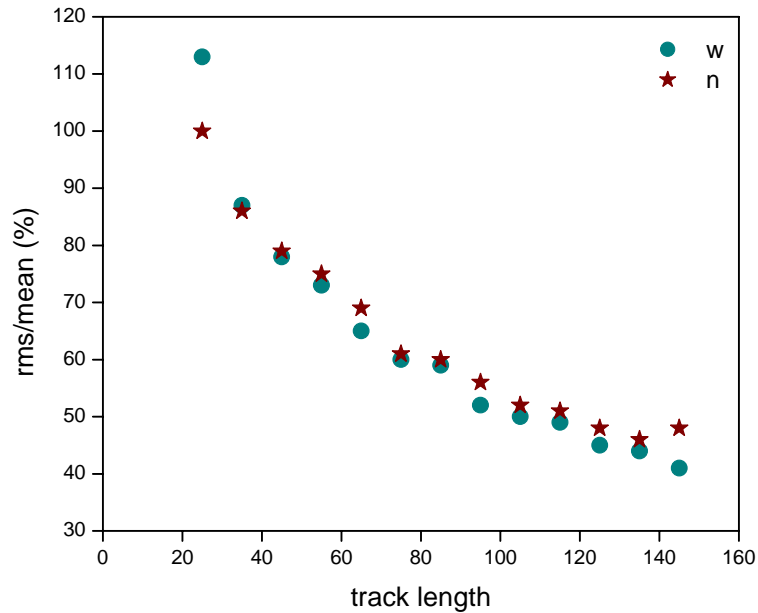West and north data are shown in sequence.

Figure 3.12: Relative widths of the pulse height distributions shown in Figure 3.11 as a function of track length. West (circles) and north (stars) data are shown together.

We seek the best fit values of λ to the west and north data using the expression $ph_i=\lambda_i l(1+\alpha_i(d_i-d_0))$ with α_i fixed to the common value of -0.58%. The results are shown in the table below.

Table 3.4

	west geometry			north geometry		
i	1	2	3	1	2	3
λ	0.74	1.00	1.20	0.86	0.80	0.92
χ^2/dof	2.3	2.6	3.2	3.2	2.2	2.6

Figure 3.13 shows the *l*-dependence of the mean value of $ph/\lambda(1+\alpha\Delta d)$. A clear linear relation is evidenced. Figure 3.14 shows the average of the three PMT distributions before and after having corrected for their track length dependence (that is before and after having divided the pulse height by the track length measured in units of its mean value). A clear improvement is visible. Yet the ratio *rms*/mean is in fact worse after correction than before (55.9% compared with 53.9% for the west data, 63.3% compared with 58.3% for the north data).
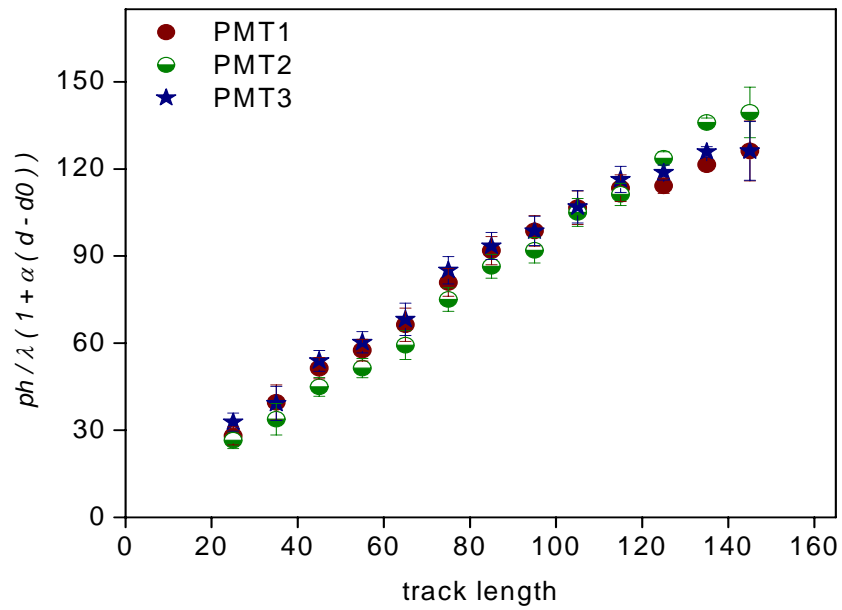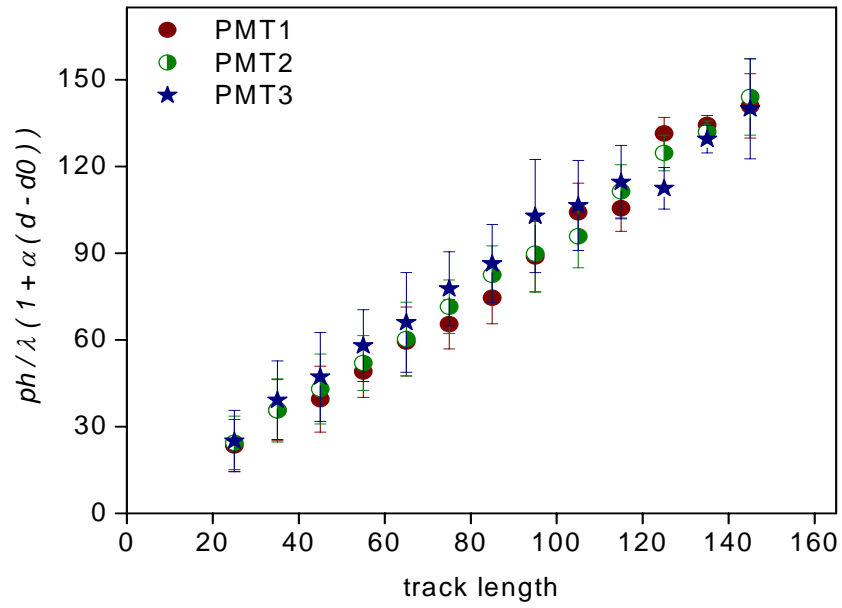
Figure 3.13: Dependence on track length of the mean value of $ph/\lambda\left(1+\alpha\,\Delta d\right)$ for the west and north data respectively.
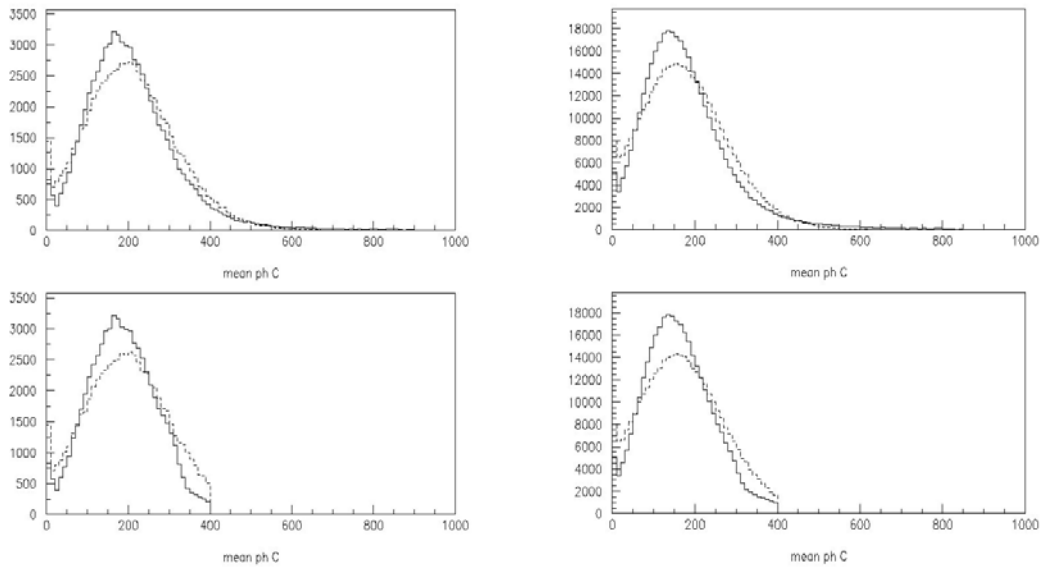
Figure 3.14: Pulse height distributions averaged over the three PMTs for the west
(left) and north (right) data respectively. Dashed lines are for raw pulse heights, full
lines are for corrected pulse heights (meaning divided by the track length measured in
units of its mean value). The lower spectra have been cut at 400 channels (see text).

The reason is the long tail at high pulse heights: if a cut at 400 channels is applied
on both spectra then the *rms*/mean ratio decreases from 48.9% to 44.1%, and 54.2%
to 49.8% respectively. It may sound surprising at first sight that the improvement is
so small, particularly when one sees the very clean results displayed in Figure 3.13.
The reason is simple: the pulse height distributions at fixed track length are already
very wide, as was shown in Figure 3.12, typically between 50% and 80%.
Moreover, the spectra are cut at low values when going to small track lengths: when
the measured pulse height is zero to start with, it does not help to divide it by the
track length! These two effects preclude the achievement of a significant
improvement after having corrected for track length.

3.4. Conclusion

The study of the Cherenkov response to atmospheric muons has shown a number of
features that may be briefly summarized as follows:

– The pulse height spectra measured in each phototube depend in a clear and
well understood way on track length and on the proximity of the track.

35

– Pulse height spectra are too wide and too low compared to what they should be. From the value of *rms*/mean=48% for vertical muons and 3 good PMTs, compared to the Auger [13] equivalent number of 15%, we deduce that we have $(48/15)^2$=10 times less photoelectrons in VATLY than in Auger. Assuming a factor 2 in photocathode efficiency and accounting for the factor 1.2 in photocathode area, we deduce a deterioration factor of 10/2.4 = 4 resulting from the lower water transparency and the worse wall diffusivity.

– The poor resolution precludes the use of an efficient correction algorithm allowing for improving it. Indeed, taking the average of the three PMT pulse heights (which boils down to increasing the collected light by an average factor of three) is the best one can do.

A parallel study [18] has shown that the PMT's suffer an important after-pulsing, most likely due to the presence of gas in the glass envelopes. This should not, however, cause an important deterioration of the resolution. The purity of the water and the quality of the diffusing surface of the tank walls are much more likely candidates to explain the low value of the light collection.

A refurbishing of the VATLY Cherenkov counter is currently underway. It includes the following steps:

– replace the EMI (very old) phototubes by new Photonis phototubes of the type used in the Auger experiment. Both the last dynode and the anode signals of each phototube are amplified and analyzed separately. This step is now completed.

– coat the inner tank walls with aluminized Mylar that should provide a better diffusion coefficient than white paint.

– improve the quality of the water transparency and prevent thin particles to settle down on the floor of the tank, deteriorating significantly its diffusivity.

Chapter 4 - THE TIME STRUCTURE OF THE SURFACE DETECTOR SIGNALS

4.1 Introduction

For each trigger the surface detector signals recorded by each of the three PMTs of a same counter are stored as a function of time in bins of 25 ns in flash analog to digital converters (FADC). Figure 4.1 shows an example of an FADC trace, the signal is represented in units of VEM (vertical equivalent muon, it is the average charge of the signal obtained for vertical relativistic muons crossing the whole water volume). The FADC signals are made of peaks associated with particles traversing the water tank or stopping into it superimposed on a small noise
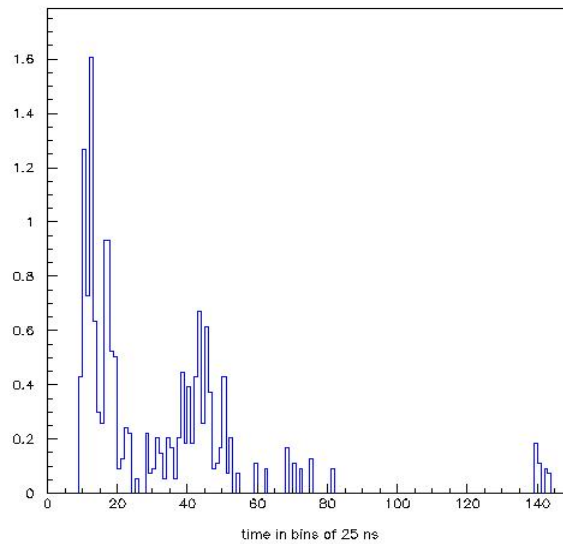
Figure 4.1 An example of an FADC trace (event Id 620791, station nr 119)

level. They are mostly produced by muons, electrons and photons (in the following, we write eγ for electrons and photons together, usually members of soft electromagnetic showers developing in the water tank). The muon signal clusters around a mean pulse height of about 1VEM – to the extent that the muon zenith angle is not too large and that it crosses the whole water volume. The electromagnetic signal has usually a rapidly decreasing distribution starting at a very low value defined by the detection threshold.

37

The muon/eγ ratio is expected to be one of the quantities that can be used to identify the primary. Because the muon lifetime is very long, most muons reaching ground originate from the early part of the shower development. On average, an iron shower starts developing earlier than a proton shower does. It is therefore expected to produce more muons at ground level. It is therefore important [19] to separate the two components for the identification of the hadronic primary. However this separation is very difficult and is in demand of further improvement.

In this chapter, we concentrate on the reduction of the FADC traces to sums of muon and eγ peaks, an essential preliminary to further studies of the shower properties. A program has been developed and tested on real shower data[5] and performs properly.

4.2 Combining the three PMT signals and defining intervals

The three PMT signals are expected to somewhat differ because they collect different samples of the Cherenkov light produced by the traversing particle(s). Such differences might be used to infer information on the nature of the incident particle(s), the location of its impact, its angle of incidence, etc…but such is not our aim in the present work. Here, instead, the three PMT signals are combined into a same common signal, using the inter-PMT differences to attach a reasonable uncertainty to the combined signal. From the observed inter-PMT differences we have evaluated an uncertainty of the form $\Delta S_i = 0.28 \times (S_i^{0.8} + 0.007)$ attached to each PMT signal S_i. This uncertainty is then used to calculate the weighted mean S* of the three PMT signals and its associated uncertainty. Figure 4.2 shows distributions of $(S_i - S^*)/\Delta S_i$ for a sample of 1500 events in different intervals of S*. The mean and *rms* values are seen to be stable as a function of S^* and to take values close to 0 and 1 respectively, as they should. In what follows, we only retain channels having a signal S* deviating by more than 3 standard deviations (3sd) from zero. We call them "on". Only when we calculate the χ^2 of our model to the data will we include channels that are not "on".

---

[5] The data was taken from January to April 2004

We then define intervals as sets of connected "on" channels. Each interval j is defined by its first and last channels, i^j_{start} and i^j_{stop}, and is given a width $w_j = i^j_{stop} - i^j_{start} + 1$ (in units of 25ns bins).

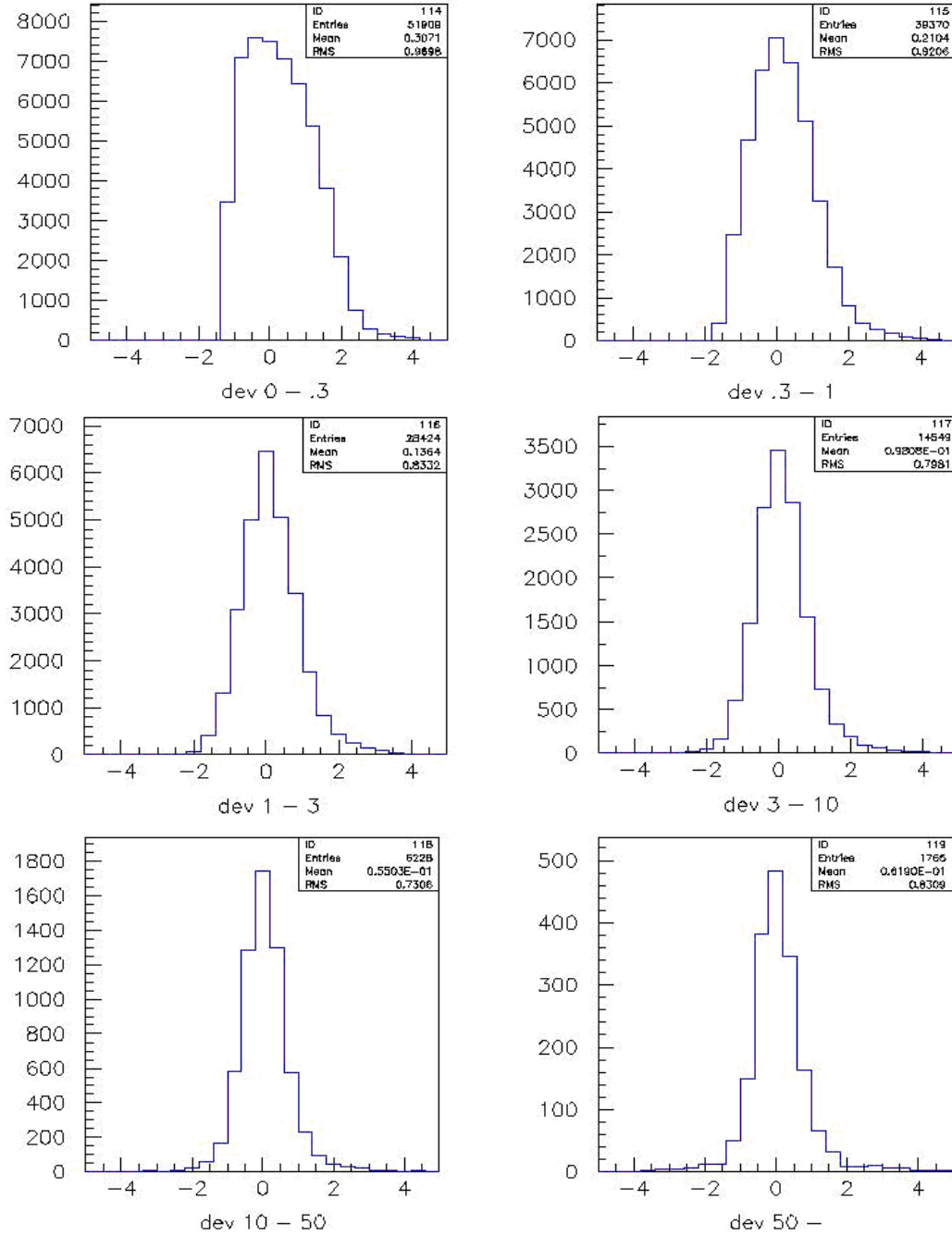

Figure 4.2: The distributions of (Si−S*)/ΔSi in six different intervals of S*
(0 to 0.3, 0.3 to 1, 1 to 3, 3 to 10, 10 to 50 and above 50).

Figures 4.3 and 4.4 show the distribution of the number of intervals in each event and that of their widths. A large fraction (49%) of intervals is only one or two channels wide.
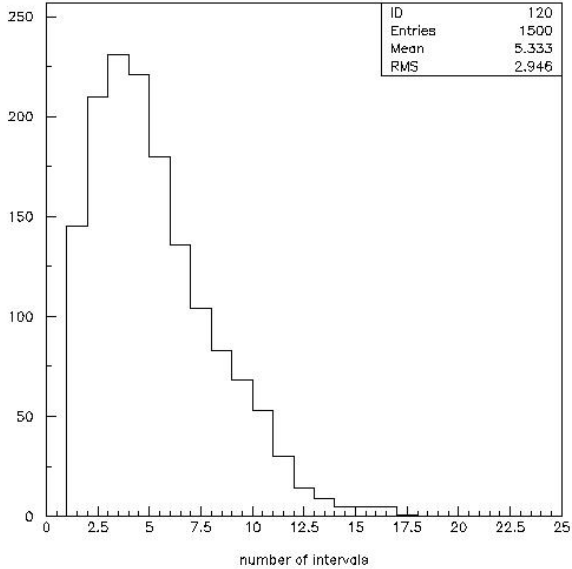
Figure 4.3: Distribution of the numbers of intervals in each event.
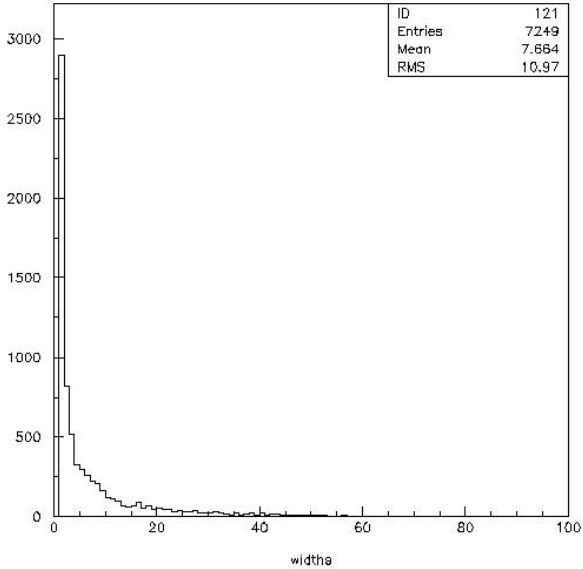
Figure 4.4: Distribution of the widths of the intervals.

The distribution of their area Σ is shown in Figure 4.5 for one-channel-wide and two-channels-wide intervals separately. The difference is artificial, due to the

cut at 3sd defining "on" channels. In both cases a small peak corresponding to an area in excess of 1 is visible, most likely corresponding to muons, and amounting to 14.3% and 10.6% respectively (13.5% in total). These narrow intervals are ignored in the peak searching procedure. The distribution of their number per event is shown in Figure 4.6.
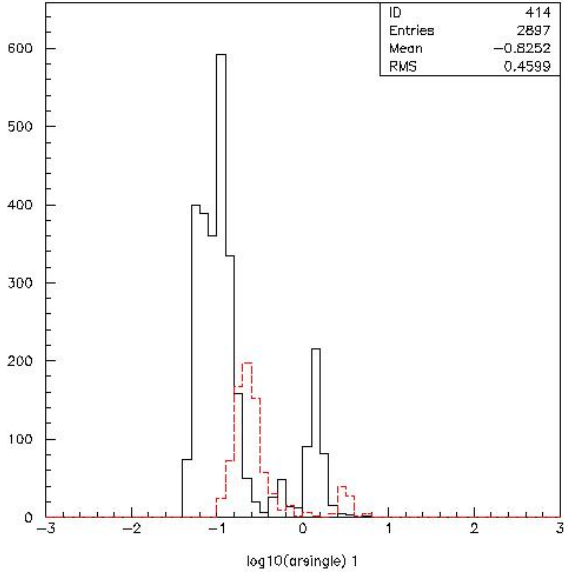

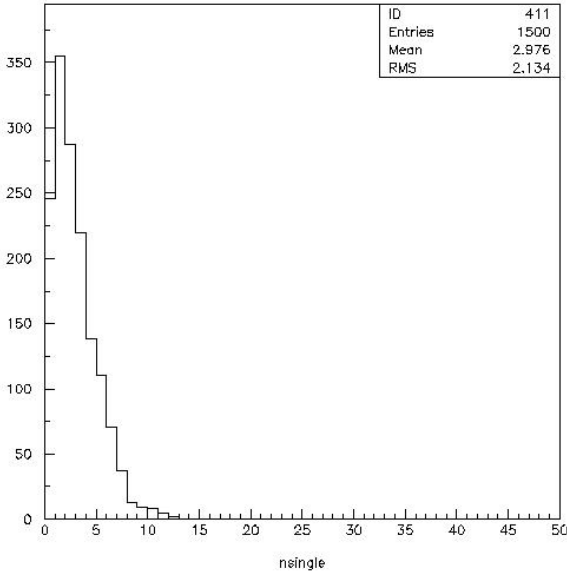Figure 4.5: Distribution of the areas of one-channel-wide (full line) and two-channels-wide (dashed line) intervals

Figure 4.6: Distribution of the numbers of single intervals per event

4.3 Peak searching

We now explore each interval looking for maxima. A maximum is defined as channel i such that its content exceeds that of channels i−1 and i+1. This definition includes maxima that are not statistically significant but we prefer to start the search with too many candidates and reduce their number later on. In the cases of the first and last channels of the interval it is sufficient to require that its content exceeds that of its neighbor in the interval. Figure 4.7 shows the distribution of the number of maxima per event (dotted line). It has a mean of 7.7 (10.2 when including intervals having a width smaller than 3 channels) compared to 2.4 (4.8), the mean number of intervals per event.
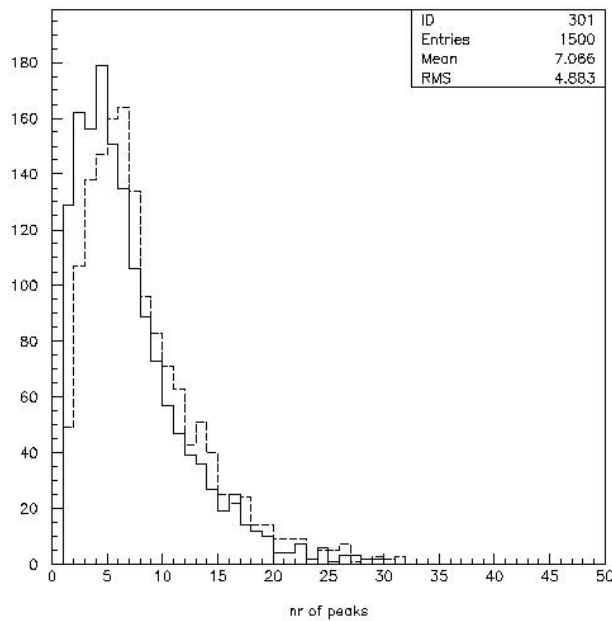

Figure 4.7: Distribution of the number of maxima per event (dotted line) and of the reduced number of maxima at the end of the minimization procedure (full line).

We then associate to each maximum a peak having a well defined shape that we have tuned in an *ad hoc* way to the data. This shape, $P(\rho)$, is illustrated in Figure 4.8 as a function of ρ. Each peak k is in fact taken of the form $H_k P[(x-x_k)/a_k]$ where the height H_k, the peak location x_k and the width a_k (the latter two measured in channels) are adjustable parameters.

The fitting procedure consists then simply in the minimization of the χ^2 that describes the deviation between the observed FADC trace and the model defined as the sum of all peaks. The χ^2 (and therefore the search for its minimum) is restricted to intervals more than 2 channels wide. However, channels located outside the interval may be included in its evaluation if the model predicts that their content exceeds .04 (this value corresponds to the definition of channels "on" in the case of the data). The uncertainty used in the evaluation of the χ^2 is either the experimental one when the channel is "on" or, when it is not, the error that would be assigned to the prediction if it were an experimental value.
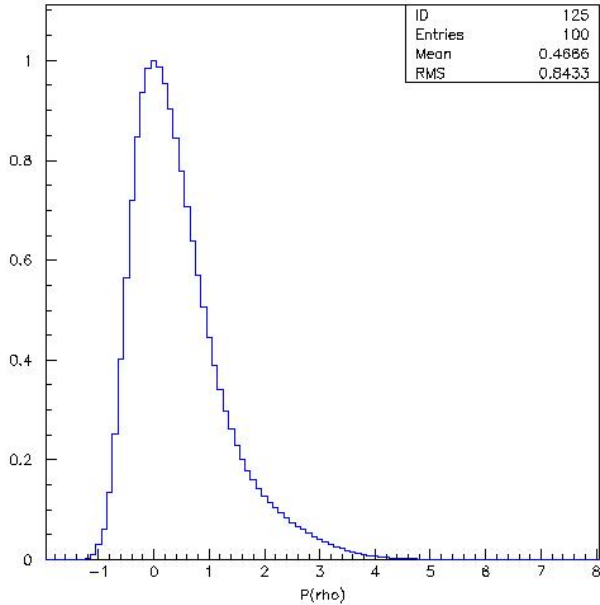

Figure 4.8: The function $P(\rho)$

We proceed by iterations. As expected, several of the peaks defined are not significant but are simple statistical fluctuations. In order to reduce, in fact nearly suppress, their contribution we discard any peak being less than three standard deviations significant, starting at iteration number 8. The significance is defined as the ratio between the sum of the predicted peak channels and its uncertainty. The choice of 8 iterations was made by studying the decrease of the χ^2 as a function of iteration number: it has usually become flat by then. We stop after 20 iterations, safely above what is necessary for the χ^2 to stabilize. The distribution of the

reduced number of maxima (at the end of the minimization procedure) is shown in Figure 4.7 as a full line.

4.4 Results.

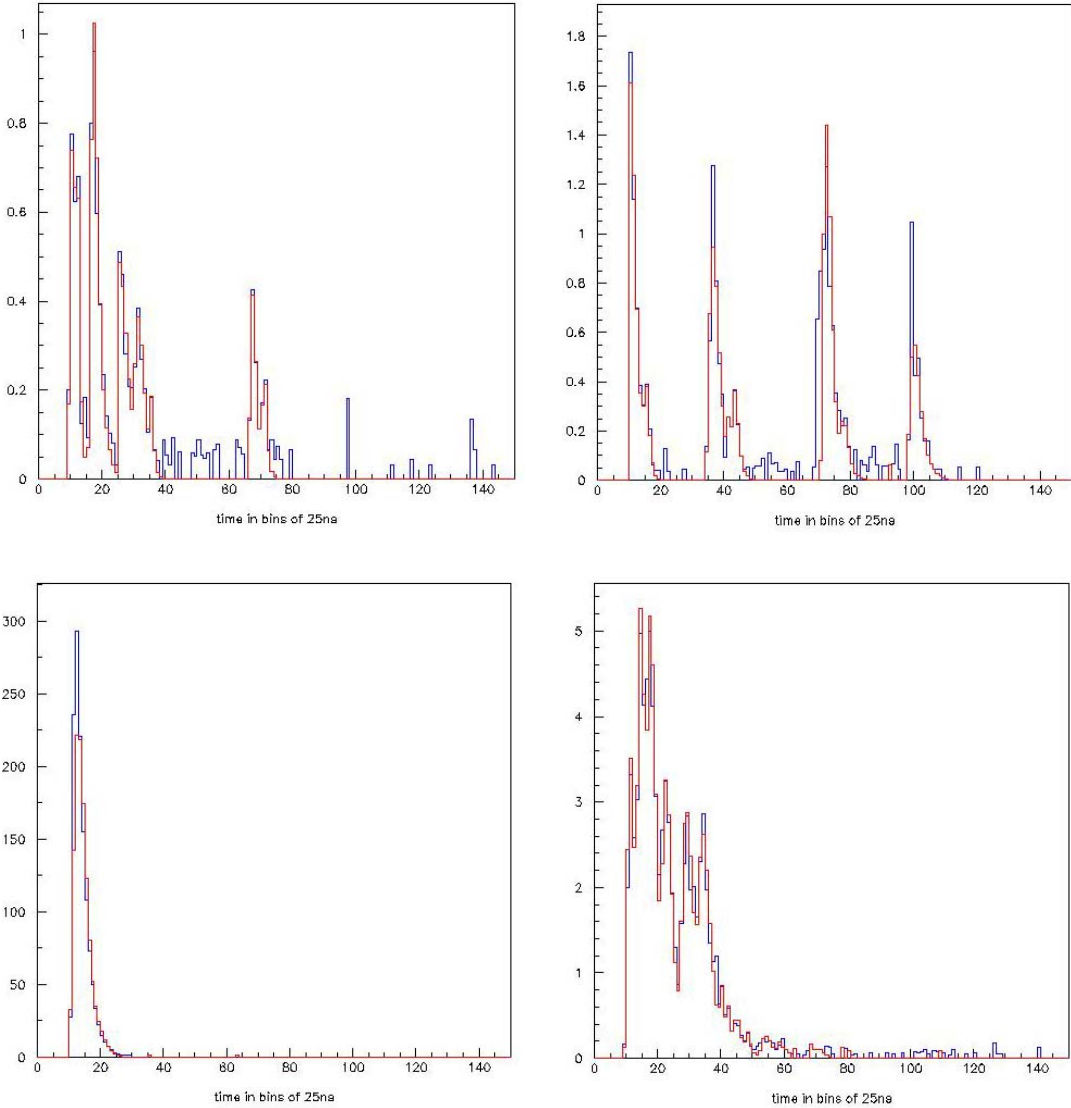Figure 4.9 shows four typical traces that illustrate the performance of the program.

Figure 4.9: Some typical traces that illustrate the performance of the program. The ordinate is in units of VEM (the blue line is the data and the red one is the fit).

The main features of the result of the fits are illustrated in Figures 4.10 to 4.14 that show distributions of respectively the χ^2/dof, the height H_k, the position x_k, the width a_k and the "area" $\Sigma_k = H_k a_k$ of peaks. The mean of the χ^2 distribution is 1.2. The height and area distributions show a clear muon peak above an eγ background starting at threshold. The x-distribution shows an artificial peak at channel 10 that results from the definition of time zero for each FADC trace. However, the subsequent peaks (when there are some) have a distribution that peaks around 30 channels and decreases smoothly, extending up to the end of the trace. Figure 4.15 shows the 2-dimensional distribution of H_k *vs* a_k where the two different populations can be seen.

In order to study this further we define a variable ξ that tells how well a peak is isolated from its neighbours: ξ is simply the smallest of $x_k - x_{k-1}$ and $x_{k+1} - x_k$. Figure 4.16 shows the distribution of ξ for all events (restricted to intervals more than 2 channels wide). The spike at 75 corresponds to events having only one such peak.

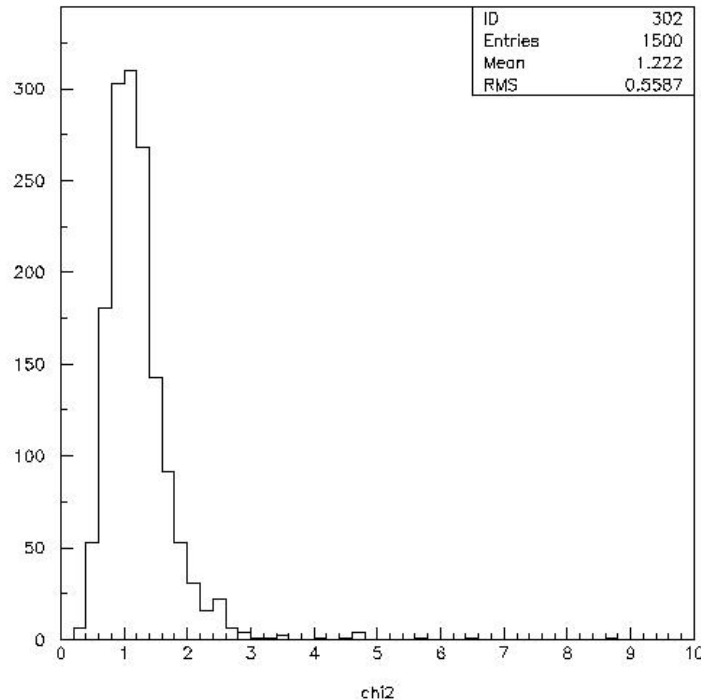| ID | 302 |
Entries	1500
Mean	1.222
RMS	0.5587

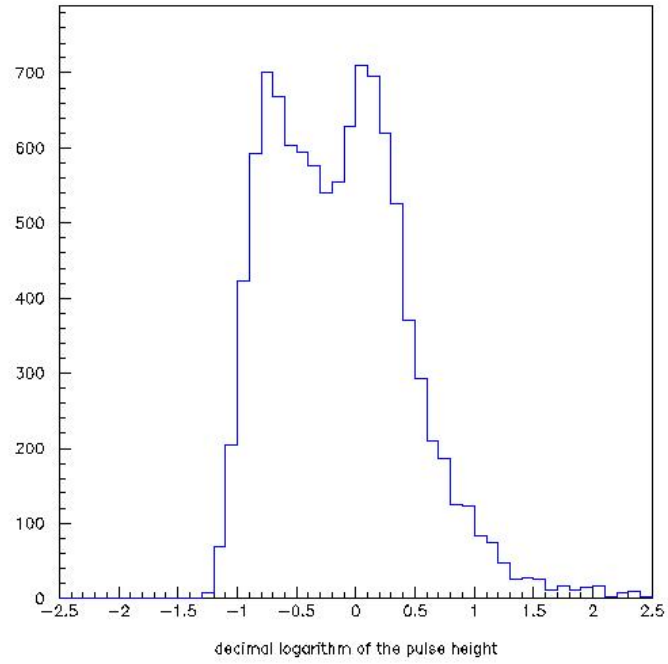Figure 4.10: The χ^2 distribution

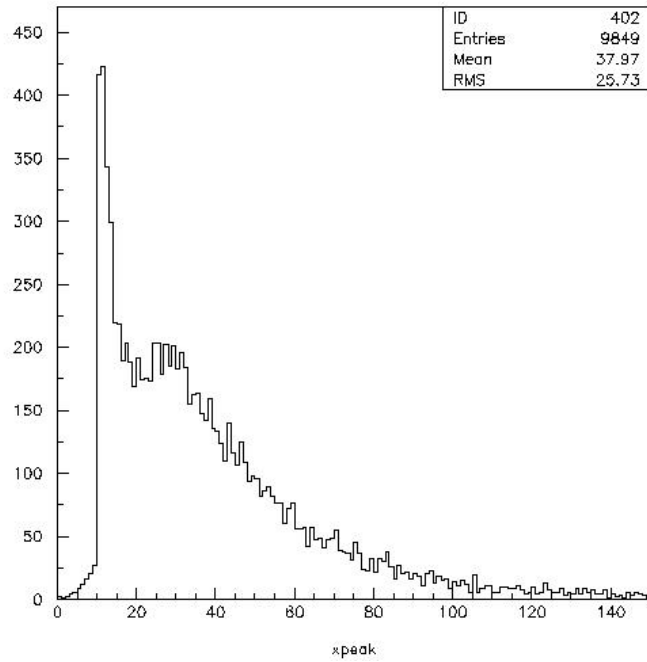Figure 4.11: Distribution of the peak heights
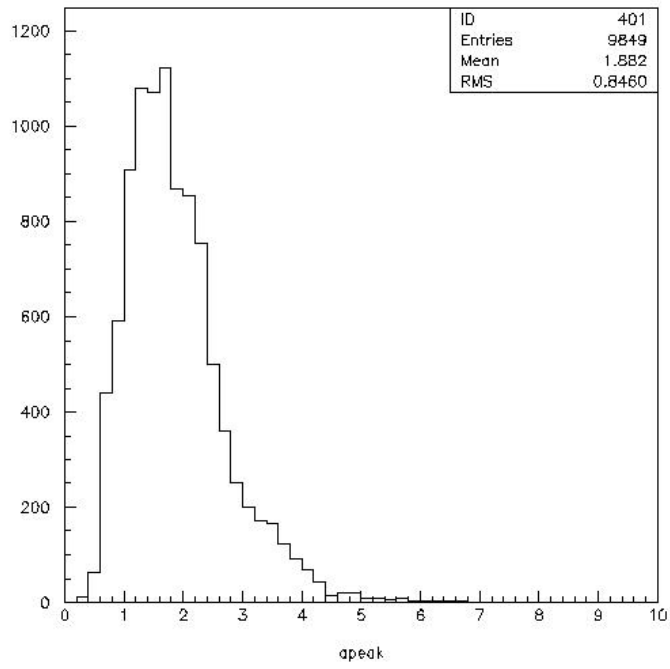

Figure 4.12: Distribution of peak positions
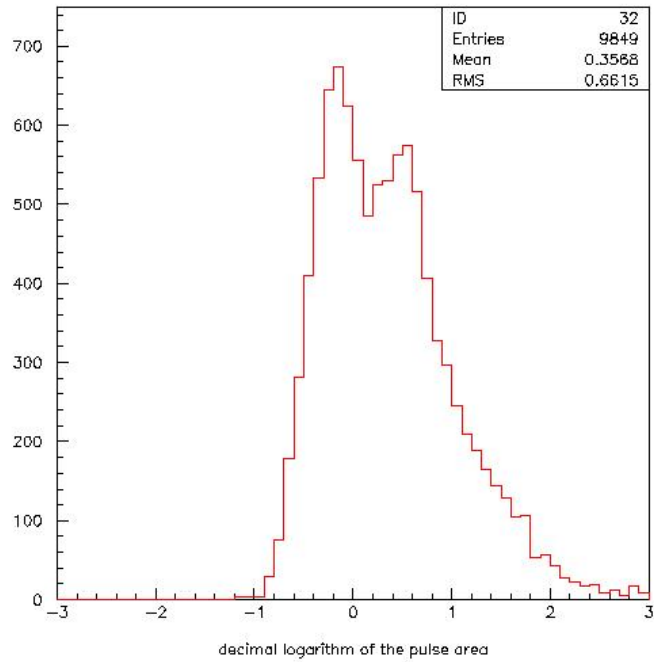
Figure 4.13: Distribution of peak widths
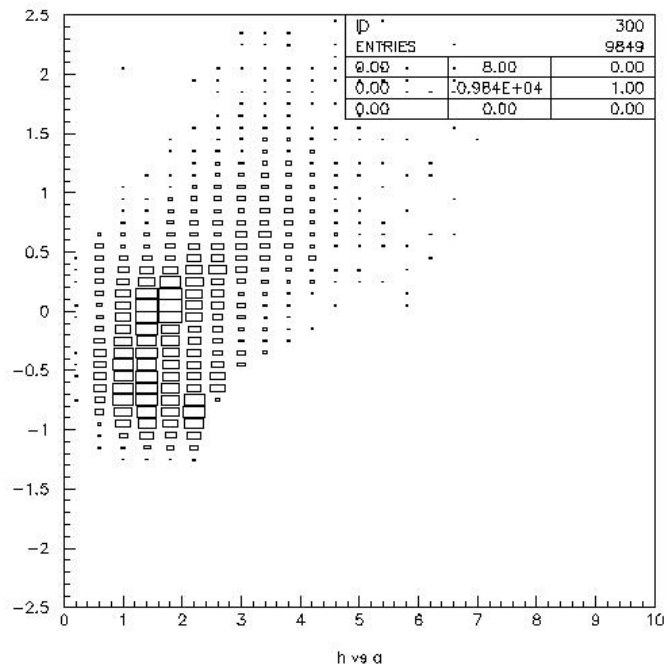

Figure 4.14: Distribution of peak areas

Figure 4.15: Two-dimensional distribution of H_k vs a_k, (the ordinate is the height H_k of the peak and the abscissa is the width a_k of that peak).
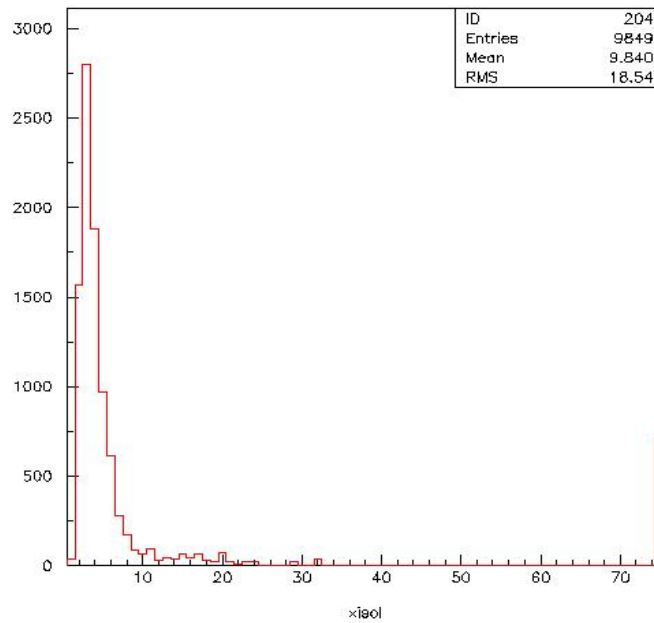

Figure 4.16: The distribution of ξ (all events)

We then show the distributions of H and Σ in Figures 4.17 and 4.18 for five different selections of peaks corresponding to different values of the isolation parameter: $\xi > 3, 5, 8, 10$ and 12. We define a muon signal region as $-0.3 < \log_{10} H < 0.5$ and two control regions as $-0.7 < \log_{10} H < -0.3$ and $0.5 < \log_{10} H < 0.9$. We then plot the peak widths a_k for each isolation selection as being the difference between that measured in the signal region and that measured in the control regions. The result is shown in Figure 4.19. The mean value of the muon peak width obtained this way is of the order of 2.1 channels and independent from the peak isolation. However its *rms* increases from 0.72 to 0.93 channels when ξ increases from 3 to 12. A more refined analysis should be made, in particular taking also into account the narrow (less than 3 channels wide) peaks in the definition of the isolation. A parallel analysis was performed recently by P. Billoir [20] and yields similar results as those presented here. However, for the time being, we shall be satisfied with the present result.
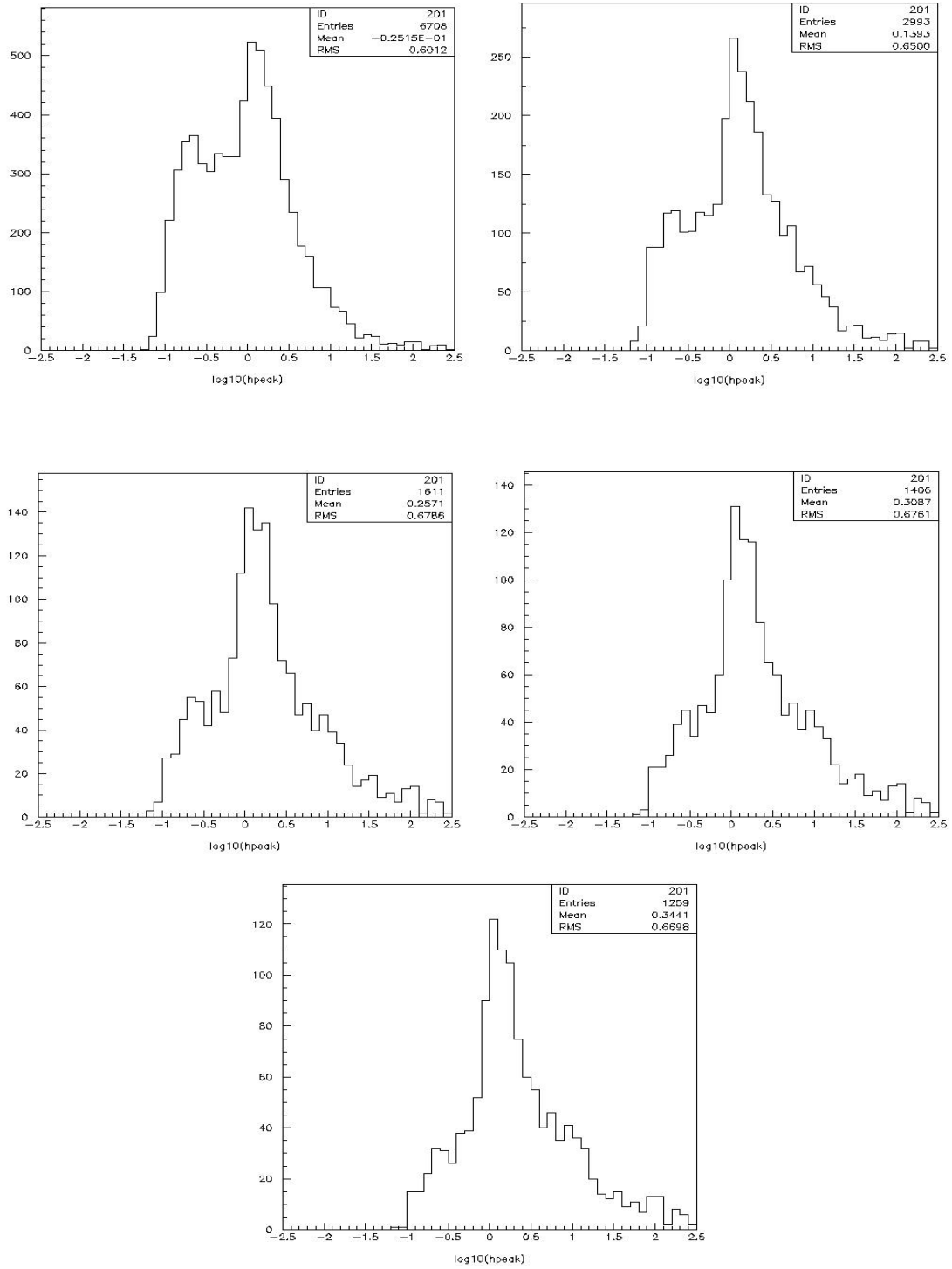
Figure 4.17: Distributions of H for different intervals of the isolation parameter ξ ($\xi > 3, 5, 8, 10$ and 12, are shown from left to right, top to bottom).

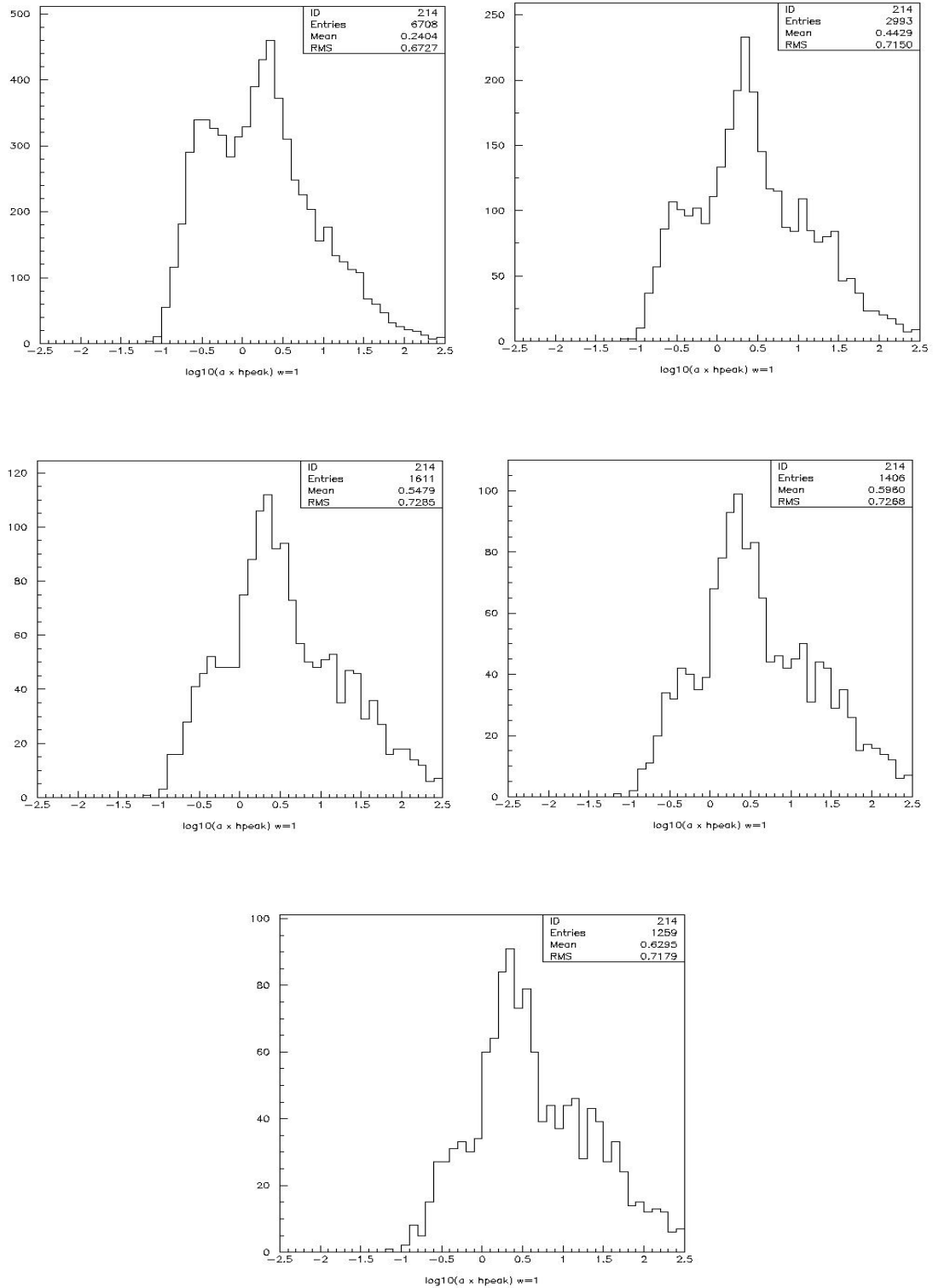Figure 4.18: Distributions of Σ for different intervals of the isolation parameter ξ
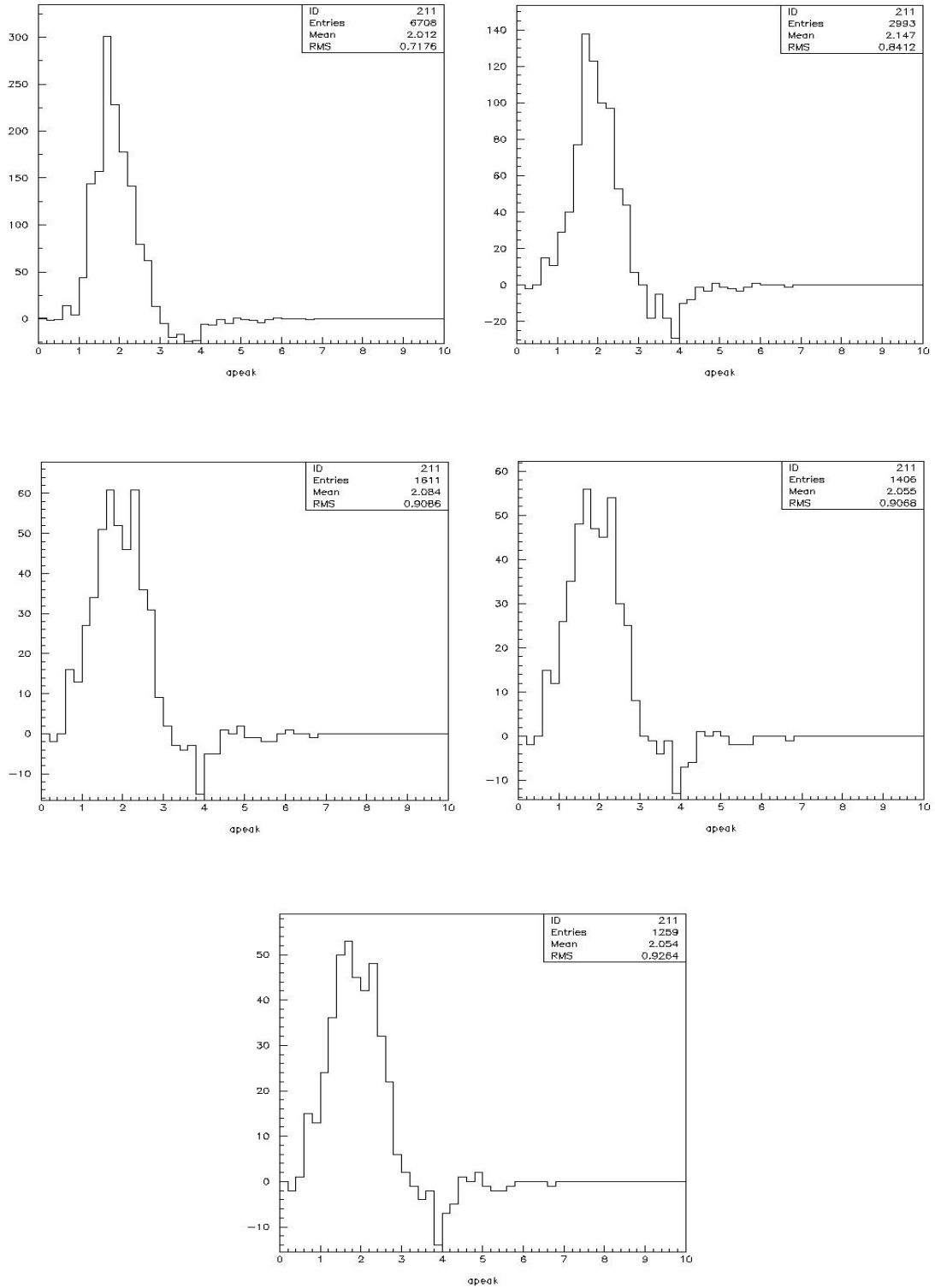(ξ > 3, 5, 8, 10 and 12, are shown from left to right, top to bottom).

51

Figure 4.19: Distributions of the peak widths a_k for each isolation selection evaluated as the difference between that measured in the signal region and that measured in the control regions.

4.5 Performance

In order to study the performance of the program we have generated events obtained by superimposing to a real event an additional peak. Depending on the size of this additional peak and on where it is added, it may be easily recognized (if, for example, it falls in between intervals) or it may hide a peak (or more) that was there before. An ideal pattern recognition would give always one additional peak as the result of the new search but, because of what was just said, we expect the new number of peaks to be possibly unchanged, or even smaller than the former. Particularly vulnerable are the very small peaks that may easily appear or disappear: a more reliable measure of the performance of the program will be obtained if we disregard the smaller peaks. These general considerations having been made, we now look at the result of this study.

Figures 4.20 and 4.21 show the distributions of the number ΔN of additional peaks found by the program when the extra peak is added in a populated region (Fig. 4.20 or in a deserted region (Fig. 4.21).

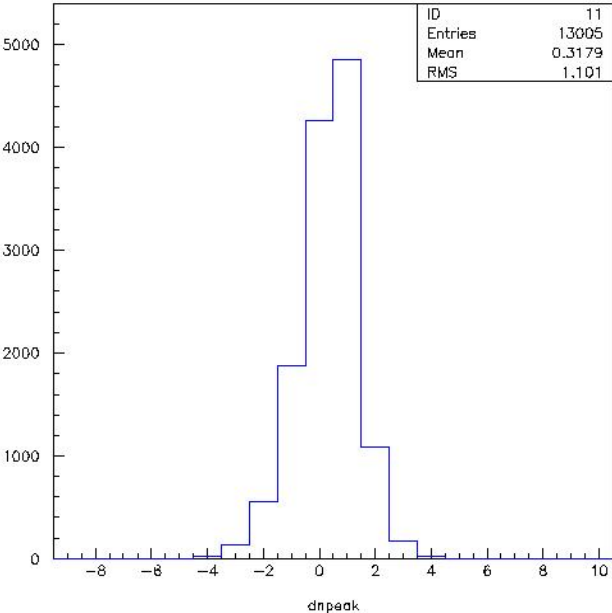| ID | 11 |
Entries	13005
Mean	0.3179
RMS	1.101

Figure 4.20: Distribution of the number of additional peaks found when a peak is added in a populated region
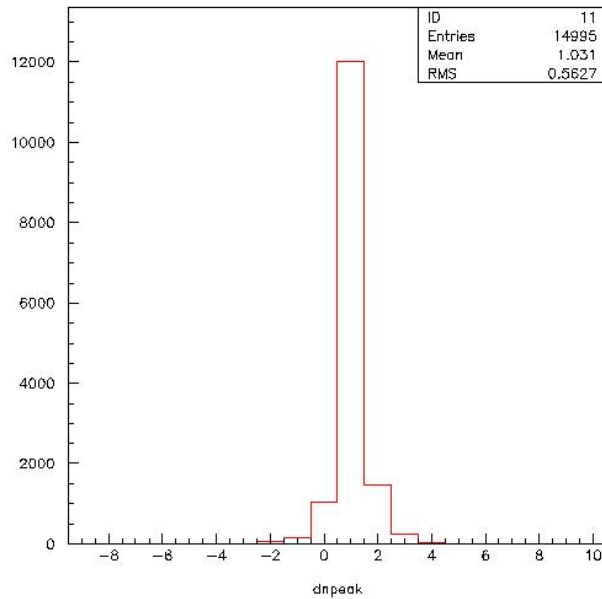
Figure 4.21: Distribution of the number of additional peaks found when a peak is added in a deserted region

In the latter case the program works well ($<\Delta N>=1.0$) but in the former it finds an additional peak in only 32% of the cases. If, however, we restrict the analysis to peaks having a height in excess of 2/3 this number increases to 72%, showing that the difficulty is with small peaks (Figures 4.22 and 4.23). Indeed, we note that when adding a peak in a deserted region ΔN is not always exactly 1. This is also true in the general case where the total number of peaks found by the program can vary by ±a few units depending on very small details, such as the initialization of the random number generator (the minimization procedure uses random searches). The number of very small peaks is very poorly defined, which is neither surprising nor bothering.

In conclusion, this rudimentary study has pointed to two difficulties inherent to the nature of the problem. One is the difficulty to identify a peak as being a muon peak on an event-by-event basis (there are many eγ peaks that look like a muon peak), a separation between muons and eγ can only be made on a statistical basis. The other is the difficulty to identify unambiguously very small peaks. None of these difficulties, however, should prevent us to pursue our analysis of ADC traces with the aim of extracting some physics information.
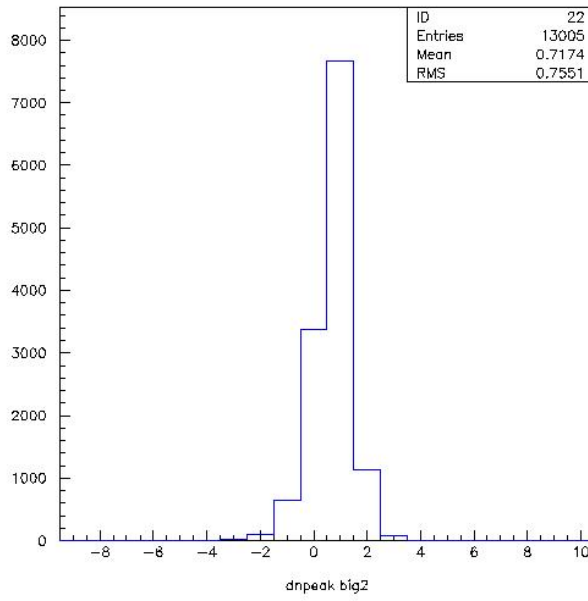
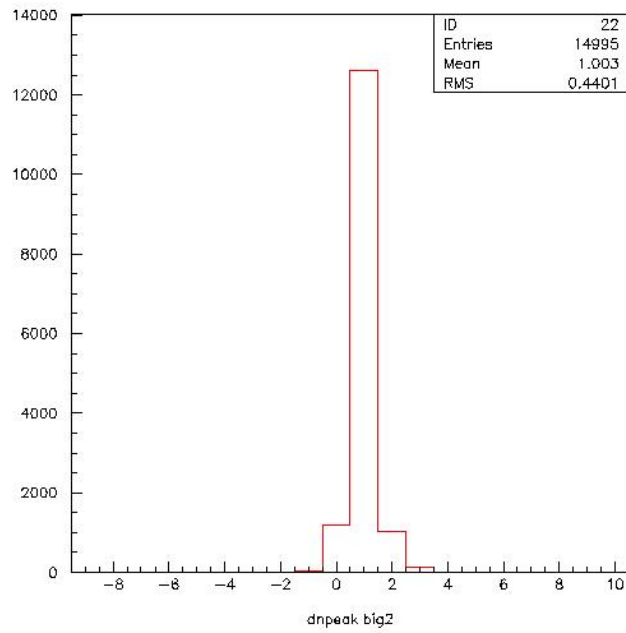Figure 4.22: Distribution of the number of additional peaks >2VEM/3 (populated region)

Figure 4.23: Distribution of the number of additional peaks >2VEM/3 (deserted region).

PERSPECTIVES

This work is part of ongoing studies aiming at having as detailed and complete an understanding as possible of the behavior and performance of the water Cherenkov counters used in the surface detector of the Pierre Auger Observatory to detect and measure ultra high energy cosmic rays.

A precise evaluation of the number of photoelectrons collected for vertical relativistic muons (VEM) is still in demand of being improved. At VATLY we are currently refurbishing our Cherenkov counter as has been described in chapter 2. In parallel we shall conduct laboratory studies on several Photonis PMT's that have been given to us for this purpose. We have also constructed an ensemble of three smaller counters that surround the main counter and that are currently being run in: they give us the ability to detect and study extensive air showers of modest energies and to study how the main counter responds to them.

The analysis presented here of FADC traces of Auger events is only the beginning of a longer study that will be the subject of my PhD thesis work. This will be done under joint supervision between Hanoi and Paris where Pierre Billoir, my Paris supervisor, is the expert of the PAO collaboration in this matter. It is difficult at this stage to ascertain what will finally be accomplished as the difficulty of the task is very large. However the interest in separating the muon and eγ components of Auger events is of primordial importance in the identification of the primary and any progress along this line will be highly welcome.

APPENDIX

Correlations between the three d_i values of a same event

Care must be exercised when working with the d_i 's because they are strongly correlated, in particular when cutting on them. In order to clarify and illustrate their behaviour, we have Monte Carlo generated a uniform distribution of impacts on the Cherenkov lower plane and calculated for each event the three d_i values. The distribution of Max(d_i) vs Min(d_i) is shown on Figure 1-A. Also shown are the distributions of the smallest, medium and largest d_i in Figure 2-A. These figures are useful tools when working with the d_i 's, in particular when deciding on a cut to apply on them.

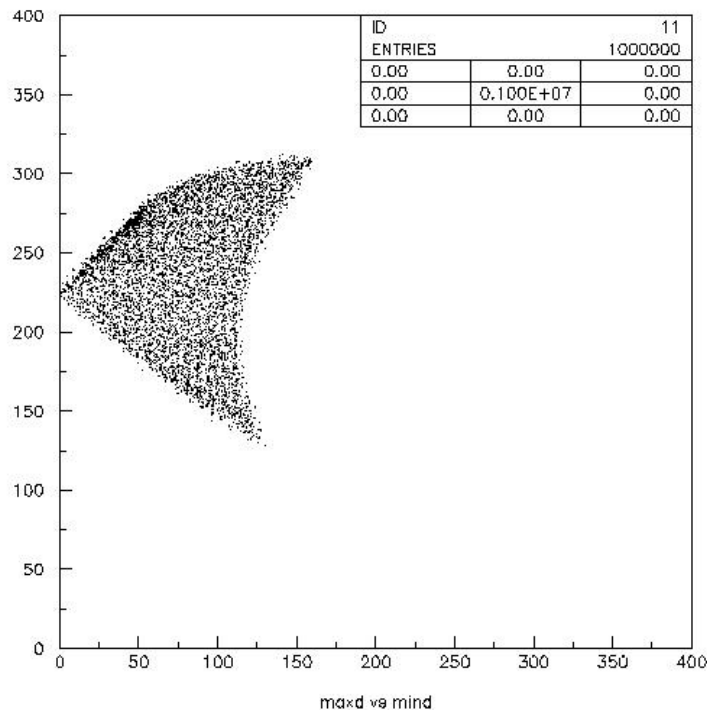| ID		11
ENTRIES		1000000
0.00	0.00	0.00
0.00	0.100E+07	0.00
0.00	0.00	0.00

maxd vs mind

Figure 1-A: Monte Carlo generation of impacts on the lower Cherenkov plane. For each event the three d_i values are calculated. The largest of the three is shown in ordinate, the smallest in abscissa.
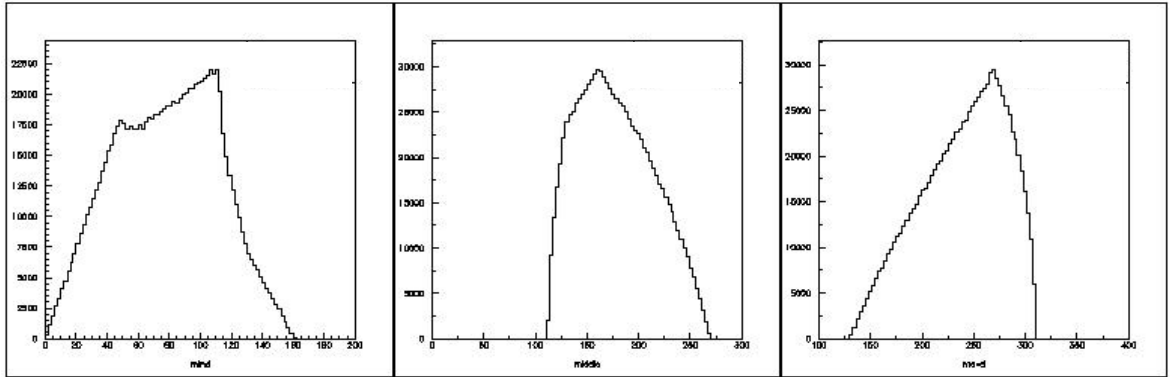
Figure 2-A: The distributions of the smallest, medium and largest d_i 's (from Monte Carlo events) are shown from left to right. Watch the different horizontal scales!

REFERENCES

[1] J.W. Cronin, Rev. Mod. Phys. 71 (1999) 165,
   J.W. Cronin, Proceedings of the TAUP meeting, Seattle, September 2003.

[2] M. Nagano and A.A. Watson, Rev. Mod. Phys. 72 (2000) 689.

[3] L.O'C. Drury, Contemp. Phys., 35 (1994) 232,
     edited by E. Parizot, and references therein.

[4] S. Yoshida et al., Astropart. Phys. 3 (1995) 105,
   M. Takeda et al., Phys. Rev. Lett. 81 (1998) 1163,
   M. Takeda, et al., in Proceedings of the 26th International Cosmic Ray Conference,
     Vol. 3 (1999) 252.

[5] D.J. Bird, et al., Astrophys. J. 424 (1994) 491.

[6] The Pierre Auger Project Design Report, The Auger Collaboration, 2nd Edition,
   Fermi Laboratory, November 1996, Revised March 1997.
     http://www.auger.org/admin/DesignReport/index.html

[7] J. Abraham, et al., Pierre Auger Collaboration, Nucl. Inst. Meth. A523 (2005) 50.

[8] P. Sommers, Astropart. Phys. 3 (1995) 349.

[9] P. Sommers et al., the 29th International Cosmic Ray Conference, submitted,
   2005.

[10] K.Greisen, Phys. Rev. Lett. 16 (1966) 748.

[11] G.T. Zatsepin and V.A. Kuzmin, JETP Lett. 4 (1966) 78.

[12] D.J. Bird, et al., Astrophys. J. 441 (1995) 144.

[13] X. Bertou, Proceedings of the 28th ICRC (Tsukuba), 2003.

[14] P.N. Diep et al., Com. Phys. Vietnam, in press, 2006.

[15] R. Urban, et al., Internal note for Auger Collaboration, GAP 2003-047,
   Sylvie Dagoret-Campagne, Auger GAP Note, GAP 2004-038.

[16] P.N. Dinh et al., Nucl. Phys., 627B (2002) 29,
   P.N. Dinh et al., Nucl. Phys. 661B (2003) 3,
   P.N.Diep et al., Com. Phys. Vietnam 14 (2003) 57

P.N. Diep et al., Nucl. Phys. 678B (2004) 3,

P.N. Diep et al., Com. Phys. Vietnam 15 (2005) 55,

[17] Particle Data Group, S. Eidelman, et al., Physics Letters B592 (2004) 1.

[18] P.N. Dong, *After pulsing*, VATLY Internal Note Nr. 12.

[19] K. Shinozaki et al., in Proceedings of the 28th International Cosmic Ray Conference, Tokyo (2003) 401 and references therein.

[20] P. Billoir, *The muon hump in real shower data from the surface detector*, Internal note of the Auger Collaboration, GAP 2005-074.

P. Billoir, *FADC trace cleaning in surface detector through a segmentation procedure*, Internal note of the Auger Collaboration, GAP 2005-074.

P. Billoir, *Estimation of muon component in showers from peak counting in surface detector FADC traces*, Internal note of the Auger Collaboration, GAP 2005-086.